Aberrant pace of cortical neuron development in brain organoids from patients with 22q11.2 deletion syndrome and schizophrenia

Sneha B. Rao[1], Francesco Brundu[2], Yannan Chen[3,4], Yan Sun[5], Huixiang Zhu[5], Robert J. Shprintzen[5], Raju Tomer[1,3,4], Raul Rabadan[2], Kam W. Leong[3], Sander Markx[6] , Bin Xu[6,*], Joseph A. Gogos[1,6,7,8 ,*]

1. Mortimer B. Zuckerman Mind Brain and Behavior Institute, Columbia University, New York, NY 10027, USA
2. Department of Systems Biology, Columbia University, New York, NY, USA
3. Department of Biomedical Engineering, Columbia University, New York, NY, USA
4. Department of Biological Sciences, Columbia University, New York, NY, USA
5. The Virtual Center for Velo-Cardio-Facial-Syndrome, Inc.
6. Department of Psychiatry, Columbia University, New York, NY 10032, USA
7. Department of Physiology and Cellular Biophysics, Columbia University, New York, NY 10032, USA
8. Department of Neuroscience, Columbia University, New York, NY 10032, USA

[*]senior and corresponding authors: bx2105@cumc.columbia.edu (B.X), jag90@columbia.edu (J.A.G)

Adults and children afflicted with the 22q11.2 deletion syndrome (22q11.2DS) exhibit cognitive, social, and emotional impairments, and are at significantly heightened risk for schizophrenia (SCZ). The impact of this deletion on early human brain development, however, has remained unclear. Here we harness organoid models of the developing human cerebral cortex, cultivated from subjects with 22q11.2DS and SCZ, as well as unaffected control samples, to identify cell-type-specific developmental abnormalities arising from this genomic lesion. Leveraging single-cell RNA-sequencing in conjunction with experimental validation, we find that the loss of genes within the 22q11.2 locus leads to a delayed development of cortical neurons. This compromised development was reflected in an elevated proportion of actively proliferating neural progenitor cells, coupled with a decreased fraction of more mature neurons. Furthermore, we identify perturbed molecular imprints linked to neuronal maturation, observe the presence of sparser neurites, and note a blunted amplitude in glutamate-induced Ca2+ transients. The aberrant transcription program underlying impaired development contains molecular signatures significantly enriched in neuropsychiatric genetic liability. MicroRNA profiling and target gene investigation suggest that microRNA dysregulation may drive perturbations of genes governing the pace at which maturation unfolds. Using protein-protein interaction network analysis we define complementary effects stemming from additional genes residing within the deleted locus. Our study uncovers reproducible neurodevelopmental and molecular alterations due to 22q11.2 deletions. These findings have the potential to facilitate disease modeling and promote the pursuit of therapeutic interventions.

Deletions at the chromosome 22q11.2 locus are the most frequent deletion in humans and present a highly variable clinical phenotype involving multiple systems. Adults and children with the 22q11.2 Deletion Syndrome (22q11.2DS) demonstrate cognitive, social and emotional impairments[1,2]. 22q11.2 deletions are also one of the strongest genetic risk factors for schizophrenia (SCZ)[3]. A number of behavioral and neuroanatomical abnormalities in children with 22q11.2DS are likely stemming from altered early brain development. Similarly, for a sizable fraction of patients with SCZ, especially ones with large effect mutations, genetic liability leads to pre-morbid dysfunction before full-blown disease onset after puberty by disturbing early brain development[4-7].

Rare and highly penetrant risk mutations provide a handle on experimentally tractable model systems needed to identify convergent neural substrates and underlying molecular mechanisms that can eventually serve as entry points to prevent or reverse disease progression. While, understanding the full chain of events leading from a risk mutation to brain dysfunction and the emergence of clinical symptoms, necessitates analysis of the intact brain in behaving animals, for mutations associated with severe neurodevelopmental abnormalities there is a need for such studies to be complemented by human experimental models that mirror prenatal states of the human brain. Forebrain organoid models provide a critical platform to dissect as well as integrate information, which would be hard to be accessed otherwise in the developing human brain[8-10].

To this end, here we analyze organoid models of the developing human cerebral cortex derived from hiPSC lines from patients with 22q11.2DS and SCZ as well as unaffected controls matched by sex and age. We showed that loss of genes within the 22q11.2 locus leads to neurodevelopmental defects characterized by retarded neuronal maturation trajectories and pervasive changes in gene expression. Transcriptional profiling underscored specific biological pathways underlying the observed abnormal neurodevelopmental trajectory, providing

mechanistic insights into the molecular pathogenesis of 22q11.2-associated clinical manifestations and into potential therapeutic interventions. The aberrant transcription program underlying asynchronous development contains molecular signatures significantly enriched in neuropsychiatric genetic liability suggesting that our findings may be generalized to other genetic causes of SCZ, especially ones with large effect mutations. The human forebrain organoid model presented here could serve as a human-specific preclinical model and a resource for further studies of the molecular and cellular pathogenesis of the 22q11.2DS.

Results

Forebrain organoids as models of the 22q11.2 deletions. To model and study the consequences of the 22q11.2 deletion in the context of early human neurodevelopment, we derived 3D dorsal forebrain patterned organoids from human induced pluripotent stem cell (hiPSC) lines from patients with canonical 3-Mb 22q11.2 deletion and SCZ using a well-established protocol[11] with high reliability of differentiation. For the analysis shown here, we employed iPSC lines from sibling pairs as well as cases and matched unrelated control pairs from the NIMH Repository and Genomic Resource. The dorsal forebrain identity and cell type composition of organoids were confirmed at DIV70 using immunostaining with FOXG1 (a forebrain marker), PAX6 and TBR1 (dorsal forebrain markers) as well as cell-type specific markers for proliferating/cycling cells (PH3/Ki67), radial glia (RG) (Nestin), intermediate progenitor cells (TBR2) and neurons [somatodendritic marker MAP2 and immature neuron marker doublecortin (DCX)] (**Fig S1a, b,c**).

Quantification of the growth rate of patient and control organoids, between DIV14 and DIV21, did not reveal significant genotypic differences in their average area and perimeter (Kolmogorov-Smirnov test, ns, n=72 control, 76 patient organoids, **Fig 1a**,**b**). We also tested whether there are alterations in neuronal activity in patient compared to control organoids using as a proxy system-wide glutamate-induced Ca^{2+} transients. Comparisons of three pairs at day

259 identified a significant decrease in Ca^{2+} peak amplitude in case compared to control cells ($P = 5.78x10^{-12}$, average number of cells per organoid: n=89 patient, n=124 control, **Fig 1c,d,e**) consistent with previous findings in monolayer cultures of both mouse and patient neurons[12,13,14]. Thus, despite the lack of overt effects in growth, patient organoids display different functional properties, validating their usefulness as a preclinical model for studying the disease mechanisms underlying 22q11.2 deletions.

To identify early neurodevelopmental disease pathways leading to disease phenotypes, dissect in more detail the various cell population alterations and directly examine genotypic differences in transcriptomic and regulatory profiles during neurogenesis and neuronal differentiation, we used single cell RNA sequencing (scRNA-seq). We profiled the cell type composition and molecular signatures of patient and control forebrain organoids at two stages: at DIV70, when organoids contain an abundance of progenitors and neurogenesis is beginning and at DIV150 when multiple subtypes of cortical excitatory neurons (EN) emerge along with interneurons and astroglia. We generated a high viability (>90%) single cell suspension for scRNA-seq from each of 3 pairs of DIV70 and DIV150 organoids, a total of 6 lines from 3 individual patients and 3 control with 3 organoids per line and developmental time points. Quality control metrics were uniform across organoids from all iPSC lines, with low counts of mitochondrial and ribosomal genes detected and comparable count metrics for all samples (**Fig S2a**). We observed negligible differences in the expression of hypoxia and apoptosis markers between patient and control organoids and between timepoints, indicating healthy organoids across timepoints and genotypes (**Fig S2b, c**). After quality control and filtering, a total of 55,762 single cells were analyzed. We identified 8 distinct cell clusters whose distribution was uniform between samples with the Leiden algorithm[15,16] (**Fig S2d**). Assessment of 22q11.2 locus genes expressed in forebrain organoids confirmed the expected ~50% reduction in all patients compared to control organoids (**Fig S2e**), indicating high consistency of the transcriptomes among samples (**Fig S2f**).

Altered cell type proportions in patient organoids. To more precisely annotate cell types observed in the scRNA-seq datasets, we used as a reference a published dataset that classifies the signature transcriptomic profiles of cell types in the developing human telencephalon at various stages of development[17]. Cell type mapping was conducted using the singleR tool[18]. By using a custom-built stratified subsampling approach (see Methods) we confirmed that 98% of cell annotations passed the threshold with high confidence. We found that the majority of cell types found in the developing human brain are represented in our DIV70 and DIV150 datasets (**Fig 2a and Fig S3**). At DIV70 our annotation strategy identified early radial glia (RG-early) and excitatory neurons (EN) as the predominant cell types. Intermediate progenitors differentiating into newborn excitatory neurons (IPC-nEN) represent the next most abundant group. By DIV150 organoids display a diversity of cell types including EN, late radial glia (RG-early), cortical as well as striatal interneurons (IN) and astrocytes. Overall, as development progresses, the fraction of EN lineage cells (RG-early, cyc-RG, cyc-IPC, IPC, nEN and EN) decreases. Importantly, while the relative proportion of EN lineage progenitors decreases from DIV70 to 150, the proportion of newborn and maturing EN remains fairly constant. Conversely, there is an expansion of IN lineage as well as astrocytes at DIV150.

Examination of the distribution of cell types in the DIV70 dataset revealed that a larger proportion of cells in the patient organoids were in the cycling progenitor clusters while a smaller proportion of cells were in the differentiated neuron clusters compared to control organoids (**Fig 2b**). Quantification of the various cell types in the EN lineage using scCODA[19] identified a trend towards a higher number of cycling progenitors and a significantly lower proportion of differentiated neurons in patient organoids compared to control (**Fig 2c**). Parallel analysis of layer thickness in DIV45 organoids, when rosette structures are prominent, produced consistent results. For each rosette, we defined the PAX6-positive neural progenitor cell layer as the subventricular zone (SVZ) and the CTIP2-positive neuron layer as the cortical plate (CP). We

found no significant change in the relative thickness of the SVZ layer, but found a significant decrease in CP thickness in patient compared to control organoids (**Fig S4a-c**).

To validate these observations, we conducted cell cycle analysis of DIV70 organoids using fluorescent activated cell sorting (FACS) of cell suspensions obtained from 3 organoids per pair and two independent batches. We labeled cellular DNA using propidium iodide and sorted the cells based on DNA content as either G0-G1 phase or active cell cycle (S-M phase). We found a trend (p=0.07) towards a higher proportion of cells in S-M phase in patient organoids (**Fig S4d,e**). Since the proportion of cycling cells among neural progenitor cells is a small fraction of total cells in the DIV70 organoids, we analyze cell cycle specifically in the neural progenitor cells. To this end, we conducted 3D immunostaining of organoids from all 3 pairs. S phase cells were labeled with a 2-hour pulse of BrDU, co-immunostaining with Ki67, a proliferation marker, to label actively cycling cells, and SOX2 to label neural progenitors (**Fig 2d**). In agreement with scRNA-seq and cell sorting data, our analysis found a significant increase in the proportion of Ki67-positive/SOX2-positive cells (neural progenitors in the cell cycle) and a non-significant increase in BrDU-positive/SOX2-positive cells (neural progenitors in S phase) in patient compared to control organoids (**Fig 2e**). There was a relative consistency across each line of the control and patient organoids showing reasonable reproducibility across organoids within the same group (**Fig 2f**). We also used FACS-based analysis to experimentally probe the reduced number of neurons in the scRNA-seq dataset by expressing green fluorescent protein (GFP) under the neuron-specific synapsin promoter using AAV1-SYN1-GFP and sorting of labeled neurons two weeks after adenoviral infection. We noted that the fraction of GFP-positive neurons was lower in patient compared to control organoids, although the difference was not significant (**Supp Table 1**) Overall, these findings raise the possibility that the 22q11.2 deletion retards neuronal maturation during early neuronal development.

22q11.2 deletion leads to asynchronous developmental trajectories in forebrain organoids. To understand whether differences in cell population frequencies result from

aberrant developmental trajectories during early neuronal development we used Monocle2[20] to examine the developmental dynamics of the affected cell types within the EN lineage in our scRNAseq datasets (**Fig S5a,b**). Plotting the cell distribution of DIV70 EN lineage along the pseudotime trajectory revealed an increased distribution of mutant cells in the early phase of the trajectory (progenitor states) and a decreased distribution of mutant cells towards the terminal phase of the trajectory (mature neuron states) (P = 1.347x10^{-11}, two-sided Kolmogorov-Smirnov test; **Fig 3a,b**), supporting delayed differentiation of progenitors as well as delayed maturation of EN in patient organoids. To corroborate with a complementary approach, we applied RNA velocity analysis using scVelo to recover directed developmental dynamic information from our single-cell transcriptomics dataset. RNA velocity analysis uses gene splicing dynamics to quantitatively measure transcriptional transition states and infer the differentiation trajectory and fate potential of individual cells. We used the CellRank pipeline[21] to order cells based on latent time as determined by the transition of RNA velocity between cell states and computed cell-to-cell transition probabilities using a Markov state model of RNA velocity and transcriptomic similarity. We defined EN as the terminal state and computed absorption probability (a measure of the probability of each cell reaching the endpoint of the lineage) and differentiation potential (a measure of the entropy around the absorption probabilities for each cell and its potential to differentiate towards the terminal state). UMAP plot of the velocity stream, generated by combining the Cellrank probabilities and latent time from scVelo[22], revealed a difference in the velocity, especially in the IPC-nEN cluster (**Fig 3c**). Computation of Differentiation Potential in DIV70 batch-corrected datasets indicated that cells in the EN lineage tend to stay in the progenitor status in patient compared to control organoids (**Fig 3d**). Taken together, these results suggest that the probability of RG or IPC cells reaching the terminal EN state in patient organoids is lower than in control organoids.

A significant lag in the patient EN development with fewer patient neurons towards the terminal portion of the pseudotime trajectory was still detectable at DIV150 (P = 2.13x10^{-4}, two-

sided Kolmogorov-Smirnov test) indicating that delayed maturation of EN persists at later developmental stages (**Fig 3e,f**). Pseudotime analysis in the IN lineage at DIV 150 similarly showed a reduced distribution of IN towards the endpoint of the developmental trajectory (P = 0.013, two-sided Kolmogorov-Smirnov test) indicating a significant delay in the differentiation of IN as well (**Fig 3g,h and Fig S5c**). Convergent effects on two neuronal lineages suggest that the 22q11.2 deletion may affect developmental timelines by acting at an earlier common progenitor stage. A delay in the differentiation of the RG-early for example, could in effect retard EN specification, but also the specification of RG-late and MGE progenitors. To test this hypothesis, we sub-grouped progenitors and examined their distribution along pseudotime in the combined DIV70 and DIV150 datasets. This analysis showed an increased distribution of cells towards the earlier progenitor states of a trajectory progressing from early and cycling RG (cyc-RG) as well as dividing intermediate progenitor cells to late RG, MGE-RG and MGE-IPC in patient organoids (**Fig 3i,j**). Thus, a defect traced back to early progenitors may impact the development trajectory of both EN and IN lineage progenitors.

Patient EN display impaired maturation signatures. The finding that neural progenitors are more likely to remain in a cycling state and fail to differentiate efficiently into neurons in patient organoids prompted us to determine whether those patient neurons that do differentiate show further impairments in their growth, by looking for impaired maturation signatures in morphological assays as well as in bulk RNA-seq. We transduced patient and control organoids with an AAV-hSYN1-eGFP virus at 50-55 days and 2 weeks later we imaged them as a whole mount for differences in neurite outgrowth. This strategy facilitated imaging of a large area of the organoid without sectioning, thus preserving 3D cell morphology (**Fig 4a**). Immunohistochemical analysis on these neurons showed that they express the somatodendritic marker MAP2 and the immature neuron marker DCX (**Fig S1c**), while single cell patch clamp experiments found that the majority of patched neurons show no action potentials or have immature firing patterns (data not shown). We quantified the number of branchpoints, number of

primary neurites and total neurite length for each traced cell. We analyzed a total of 8-11 organoids per line over 3-4 separate batches generated on different dates. A total of 66-166 cells per iPSC line were analyzed. We observed a marked reduction in the neurite complexity of the patient organoid neurons compared to control, with a significant reduction in all neurite complexity indices (**Fig 4b**). Importantly, these differences were reliably observed in each of the individual patient/control pairs (all three pairs analyzed above and one additional case and matched unrelated control pair, **Fig 4c**). A combined analysis revealed that the reduction in neurite complexity in patient organoids was highly significant with respect to number of branchpoints (t-test, P = 0.013, **Fig 4b,** left), neurite length (t-test, P = 0.0209, **Fig 4b**, center) and number of primary neurites (t-test, P = 0.0038, **Fig 4b**, right). In sum, patient neurons during early forebrain development present stunted neurite growth indicative of delayed maturation.

In parallel assays, we used the same set of patient and control organoids (8-10 organoids per line, 4 patient and 4 control lines) transduced with the AAV-hSYN1-GFP virus to isolate GFP-positive neurons using FACS and conduct bulk RNA sequencing on sorted neurons for molecular signatures consistent with delayed maturation. Our analysis revealed 241 genes (143 significantly downregulated and 98 genes significantly upregulated) that were differentially expressed between patient and control neurons ($Padj$ < 0.05, Log fold change >0.5, **Fig 4d**). We proceeded to annotate the function of the differentially expressed genes (DEGs) performing Gene Ontology (GO) enrichment analysis. Of the downregulated genes, the GO terms were predominantly related to neuron projection development and differentiation as well as to protein localization in dendrites, axons and synapses (**Fig 4e**) (**Supplemental Table 1**). Among the upregulated genes, the GO terms enriched were related to the secretory pathway, with protein localization in endoplasmic reticulum and Golgi apparatus (**Fig 4f**) (**Supplemental Table 1**). We also employed synaptic gene ontologies to search for signatures of impaired maturation of synaptic functional pathways among DEGs using the SYNGO tool[23]. We found significant

enrichment of synaptic genes among the downregulated genes [22 of the 143 transcripts with decreased abundance in patient neurons possessed a synaptic process annotation in SynGO (P = 5x10^{-5}), with a particular enrichment for transcripts with presynaptic/synaptic vesicle functions (GO:0045202/GO:0098793, P = 0.0331), but no significant enrichment of synaptic genes among upregulated genes, indicating that there may be a delay in synapse maturation (**Fig 4g**). The identified molecular signatures support our observation of curtailed development of patient EN and support the notion that progenitors in the developing patient forebrain fail to differentiate timely into neurons.

Aberrant gene expression underlying altered EN developmental trajectories. We used the MAST differential expression analysis[24] to identify DEGs across the EN lineage that may contribute to the aberrant unfolding of neuronal development. Gene expression profiling and functional enrichment analysis identified several genes and genetic pathways important for brain development and function that are altered in patient compared to controls, across various cell types and developmental stages, clearly indicating that the pace of early embryonic neuronal development of mutant organoids is not properly orchestrated at the gene expression level (**Fig 5 and Supplemental Tables 2, 3**). For example, genes upregulated in patient DIV70 cyc-RG (such as CCNF, KIF20A, KIFC1, TUBA1C, KIF18B, TOP2A, CKAP2, CDCA2, CCND2, CDC20), are primarily involved in the regulation of the cell cycle and promotion of cell division whereas downregulated genes (such as *PTN, CDC42, STMN4, EFNB1, EMX2, VEGFA, MAP4, SOX6, POU3F2, PAK3*) are involved in neurogenesis and neuronal differentiation, underscoring how, already at early stages of development, 22q11.2 locus haploinsufficiency alters the transcriptional regulation of progenitor proliferation and differentiation (**Fig 5a,b** and **Supplemental Tables 2, 3**). By contrast, genes upregulated in patient DIV70 EN are significantly enriched for functions related to negative regulation of neurogenesis and neuron growth and guidance pathways (such as *EPHA4, MAP4K4, HES4, LHX2, NTRK3, SEMA6A*) while downregulated genes are primarily involved in neuronal differentiation and maturation

pathways (such as *PAK3, RBFOX2, NRP2, FZD3, ANK3, CALR, RTN4*) (**Fig 5c,d** and **Supplemental Tables 2, 3**). Furthermore, as differentiation unfolds in DIV150, patient EN display consistent signatures of impaired maturation as reflected by a lower abundance of transcripts related to neuron migration, maturation and synaptic function (such as *SEMA6A, DAB1, COUPTF-1, SYN10, SYNPR*) and higher abundance of transcripts that are typically produced during periods of active neuronal growth (such as *STMN2, CNTN1, MAPT*) (**Supplemental Tables 4, 5**).

Similar results were obtained by analysis of transcriptional regulatory networks using the pySCENIC pipeline[25]. Transcription factor (TF) regulons with lower activity in patient cyc-RG are related to nervous system development and neurogenesis. In the EN cluster, TF regulons with lower activity in patient organoids are related to more mature stages of neuron development, neurite growth and synaptic function (such as *SNAP25, STMN2, NRXN1, MAP1B, ANK3, MAPT, CRMP1*), while regulons with higher activity include TFs that are typically abundant and active during early neuronal development stages (such as *LHX2, NEUROD2, SOX4, SOX11, TCF4, FOXG1, POU3F3*) (**Supplemental Table 6**).

To obtain a more unbiased evaluation of the genetic ensembles underlying the observed digression from proper developmental trajectories we performed co-expression analysis on EN lineage cells from DIV70 control organoids using a scWGCNA pipeline[26]. We identified 10 distinct WGCNA modules. Based on the number of cells expressing the modules and module size, we narrowed down our analyses to 4 modules (**Fig 5e, f**) (**Supplemental Table 7**, modules 2, 3, 4 and 9). The largest modules (modules 2 and 9) contain multiple genes that are highly expressed in neural progenitors and are associated with cell cycle regulation. Genes in modules 3 and 4 are related to neuron development, neurite outgrowth and cytoskeleton dynamics and are highly expressed in differentiated EN (**Fig 5f**). Comparative scWGNCA showed that these modules are preserved in the patient EN lineage but may have differences in

expression, density and connectivity. We computed a module score for these gene sets based on their expression level within the EN lineage cells in case and control to indicate if the module is up or downregulated. We further fitted the scores to a linear model with genotype as the predictor, each individual line and batch as the random variables. We found that both progenitor modules (2 and 9) were significantly upregulated (P = 0.002 for module 2 and P = 0.03 for module 9) in patient compared to control organoids (**Fig 5g**), further supporting our findings that progenitors in patient organoids are more likely to remain in a cycling state. Consistent with pseudotime progression, neuronal modules 3 and 4 were downregulated in patient organoids compared to control, although the difference in the module score was not significant. Interestingly ~21% and 11% of genes in modules 3 and 4 respectively overlap with the DEGs detected in EN. Similarly, ~22% and ~34% of genes in modules 2 and 9 overlap with the DEGs detected in cyc-RG suggesting that a substantial portion of DEGs contribute to the key co-expression modules in these cell types. In sum, a sizable portion of the genes in each of these control WGCNA modules are dysregulated in patient organoids, indicating a marked dysregulation in the expression of crucial gene expression networks involved in neuronal maturation due to the 22q11.2 deletion. This data provides further evidence that ensembles of genes important for neuron development are dysregulated in progenitor cells of patient organoids, in a pattern consistent with our observation that the presence of 22q11.2 deletions impedes the pace of early embryonic neuronal development.

22q11.2-associated genes and genetic pathways underlying altered development. We further evaluated the genes and genetic pathways within the 22q11.2 locus that contribute to the altered early neurodevelopmental trajectories in patient organoids. We first examined the dysregulation of microRNAs (miRNAs) as a potential mechanism for the asynchronous expression of maturation-associated genes. We have previously shown that 22q11.2 deletion results in brain-enriched miRNA downregulation and an upregulation in target gene expression due to (i) hemizygosity of *DGCR8*[27,28,], a component of the “microprocessor” complex that is

essential for miRNA production and (ii) hemizygosity of miRNA genes residing within the deletion[12,28, 29]. To assess the contribution of miRNA dysregulation to our observed cellular and RNA-seq phenotypes we performed bulk miRNA sequencing on suspension from 3 pairs of 8-10 DIV70 organoids. We identified 19 miRNAs that were significantly differentially expressed in patient vs control organoids (**Fig 6a**) (**Supplemental Table 8**). Of these, 15 miRNAs were significantly downregulated in patients (*Padj* < 0.05) (**Fig 6a**) (**Supplemental Table 8**)**,** including *hsmir-185* that resides in the 22q11.2 locus. We used the mirNet 2.0 tool[30] to perform target enrichment and network analysis for these downregulated miRNAs and found 10 miRNA target clusters (**Fig 6b**). GO term enrichment analysis on this target interaction network identified categories encompassing cell cycle-related functions (**Fig 6c**), suggesting a contribution of altered miRNA signaling to the aberrant cell cycle programming in patients.

Reduction in miRNA expression levels is largely associated with up-regulation of target genes. Consistently, in cyc-RG, the major cycling neural progenitor population in our dataset, we found that predicted target genes of downregulated miRNAs have a significant overlap with the cell cycle and proliferation genes that are upregulated in cyc-RG of patient organoids (24% of upregulated genes are putative miRNA targets, **Supplemental Table 8**). No common cellular/molecular processes are enriched among predicted miRNA target genes downregulated in cyc-RG. Functional enrichment analysis of miRNA targets overlapping with upregulated DEGs along the entire EN lineage trajectory identified additional GO terms in early RG ("RNA metabolism" and "gene expression"), intermediate progenitors (“RNA metabolism” and “neurogenesis”) and EN (“RNA metabolism" "gene expression" and "neurogenesis). Interestingly, many of the upregulated EN DEGs that are predicted targets of the affected miRNAs are identified as negative regulators of neurogenesis or are associated with more immature neurons (such as *EPHA4, KDM1A, KIF5B, MAP4K4, NTRK3, PAX6, SLITRK5, SOX11, SOX4, TCF4, VIM*). No significant GO terms enrichment was observed among

downregulated DEGs that are predicted targets of affected miRNAs in all these cellular populations (**Supplemental Table 8**).

We also tested the overlap between miRNA target genes and those in the DIV70 neural progenitor WGNA modules upregulated in patient EN lineage (**Supplemental Table 8**). We found that 20% of module 2 and 26.5% of module 9 genes are predicted targets of the downregulated miRNAs. This overlap was significant for module 9, which is associated with regulation of proliferation (P = 0.04, 1000 permutations). These results suggest that miRNA dysregulation may drive the dysregulation of genes that maintain progenitors in a cycling state and may impede their differentiation.

We evaluated disparities in temporal trajectories of miRNA targets between patient and control organoids. Trajectory differences due to compromised miRNA control can be generated by genuine increase or failure to decrease transcript abundance. We looked at the expression trajectories of DEGs in EN lineage cell types that were also identified as target genes of downregulated miRNAs along the latent time. We identified 3 main patterns of trajectory divergence between patients and controls **(Fig 6d**). First, genes that are upregulated in patient progenitors and remain upregulated over time as exemplified by *EMC10* (a regulator of membrane protein trafficking whose upregulation impedes the acquisition of full neuronal functionality in patient neurons and animal models[12,29,31]) and *PEG3* (a cell cycle regulator that is typically highly expressed in progenitor cells but not in differentiated neurons[32]). Second, genes that show upregulation in progenitors but the changes dissipate over time as exemplified by *TCF3* (a WNT signaling antagonist that increases neural progenitor cell self-renewal and represses neuronal differentiation[33,34]). Third, genes that show an upregulation at intermediate or late developmental time points but not at early progenitors as exemplified by *MAP4K4, SOX11* and *TCF4* (genes shown to inhibit neurite growth in differentiated neurons[35,36]).

Finally, we estimated in an unbiased fashion, the contribution of additional 22q11.2 genes to the signaling pathways and networks underlying the affected biological processes. We first derived a Protein-Protein Interaction (PPI) network of all DEGs (see Methods) for each affected cell type using the STRING database[37]. We conducted a centrality analysis of each PPI network to rank the relative importance of each node using centrality scores (see Methods) and determined the 22q11.2 genes that are important for the network. For the PPI network in dividing RG, we found that RANBP1[38] and HIRA[39] had higher scores. For the PPI network in EN, we found PI4KA [40]and HIRA as the highest-scoring genes (**Fig 6e**). Despite limitations of this approach (i.e proteins such as DGCR8 that exert their effects via transcriptional and translation regulation instead via interacting with other proteins may not be weighted equally in the network), these results suggest that alterations in discrete sets of 22q11.2 genes are involved in deviations of protein interaction networks that contribute to distinct cellular and temporal aspects of neurodevelopmental trajectories. Overall, our analysis supports the notion that the high risk of atypical early neuronal maturation programs in patients is the result of concerted (parallel and sequential) actions of multiple genes on focal mechanisms instead of the effects of a single gene or pathway deficit.

Aberrant gene expression in EN lineage displays signatures of neuropsychiatric genetic liability. The growing appreciation that childhood neurodevelopmental disorders and the early developmental antecedents of SCZ may share genetic liability[41] prompted us to ask whether the aberrant transcription program underlying impaired maturation contains relevant genetic signatures. Specifically, we asked if the aberrant transcripts in the EN lineage of patient organoids involve genes identified as harboring rare coding damaging variants in exome sequencing analysis of patients with SCZ, autism spectrum disorders (ASD) and developmental delay/intellectual dysfunction (DD-ID). To achieve adequate statistical power, we analyzed DEGs in cell clusters with at least 100 DEGs at both DIV70 and 150 using the DNENRICH pipeline and curated reference patient datasets (see Methods) for genes carrying rare LoF

variants, including genes very likely to be intolerant to LoF variations as measured by the probability of LoF intolerance (pLI) score[42], which ranks genes from most mutation tolerant (pLI = 0) to most intolerant (pLI = 1) and is widely used to prioritize candidate disease genes. Genes carrying rare synonymous variants were used as a control.

Our rare-variant burden analyses showed that alterations in the expression of genes harboring LoF variants display significant overlap with a wide range of cell types in the EN lineage, especially at later developmental stages (**Fig 7**). Notably, DEGs harboring LoF variants in SCZ cases are most consistently enriched in EN (including genes such as *GRIA3, BOD1L1, EIF2S3, FABP7, POTEF, SLITRK5, ZMYM2, ANKRD12, DNAM3,* KDM6B) whereas DEGs harboring LoF mutations in ASD are most consistently enriched in neural progenitors (IPC-nEN) (**Fig 7a)**. For all three disorders, the set of highly mutation intolerant (pLI≥0.9) DEGs harboring rare LoF variants displays a wider cellular representation within the EN lineage. (**Fig 7b)**. As expected, enrichment signals are absent for synonymous variants (**Fig 7c)**. Our findings suggest that during early brain development transcripts dysregulated in differentiating neurons of 22q11.2 deletion carriers are enriched for products of genes that when mutated increase the risk for SCZ and neurodevelopmental disorders.

DISCUSSION

In this study, we developed forebrain organoids from iPSCs derived from patients with 22q11.2DS and SCZ. To reduce noise among patient lines carrying a mutation with variable disease penetrance and clinical manifestations, we employed iPSC lines from patients with the same 3Mb deletion and similar severity in their clinical diagnosis. We also included in our analysis genetically related and age-matched sibling pairs. Examination of the distribution of cell types using scRNA-seq analysis and experimental validation indicated that there was a delay in neuronal maturation in the organoids during a period of active neurogenesis (DIV70 and 150 of organoid development, which strongly correlates with fetal human telencephalon

development during 7-37 weeks post-conception)[43]. Specifically, neural progenitors were more likely to remain in a cycling state and fail to differentiate efficiently in patient-derived organoids. Those that did differentiate displayed further impairments in their maturation that were reflected at multiple levels of our analysis. We found a higher fraction of actively proliferating neural progenitor cells and a lower fraction of more mature neurons in patient-derived organoids. We also found consistently perturbed molecular signatures of neuronal maturation in the organoids. In addition, the patient-derived organoids had sparser neurites and blunted amplitude of glutamate-induced calcium transients. Demonstration that patient and control organoids recapitulate the expected 22q11.2 gene expression profile as well as convergence of molecular and cellular level analyses across different batches of organoids argues against random developmental skews as a source of the observed aberrations.

Within 22q11.2DS, regionally specific differences in brain development may partially underpin behavioral alterations. In that regard, the timing, magnitude and spatial distribution of delayed neuronal maturation likely lead to regional changes in brain structure, connectivity and activity patterns early in the course of brain development. These changes may propagate to later prenatal and postnatal stages and, by affecting the regulatory robustness of neural networks, may contribute to the behavioral and cognitive symptoms that emerge due to the 22q11.2 deletions. Brain imaging studies in children with 22q11.2 deletions report alterations in thickness in several brain regions, alongside consistent decreases in surface area[44-48]. Given that during brain development, thickness is associated with progenitor divisions while surface area is associated with neuron growth and neurite branching, it is possible that the altered proliferation and expansion of progenitor cells coupled with impaired neuronal growth and differentiation (as observed in patient organoids) could contribute to the reported alterations[49-53].

Our study found convergent effects of the 22q11.2 deletion on two neuronal lineages (EN and IN). Analysis of cell distribution along the pseudotime trajectory indicates that the effect of 22q11.2 deletion on delaying the pace of neuronal maturation may initiate before the onset of

neurogenesis, as early as during the radial glia stage. Additional effects along the temporal progression from neural precursors to post-mitotic neurons may impede acquisition of full morphology and neuronal functionality[14]. This interpretation is consistent with recent findings that the rate at which human neurons mature is set well before the onset of neurogenesis through the establishment of a “barrier” in progenitor cells, comprising multiple families of chromatin regulators, that propagates to newborn neurons[54]. In the context of SCZ, the major psychiatric manifestation associated with 22q11.2 deletions, our findings are also consistent with reports of aberrant neural progenitor cell proliferation and impaired differentiation, from studies in SCZ patient neuronal models[55]. They are, however, in sharp contrast with recent findings of accelerated maturation of the same cell classes, observed in brain organoid models carrying mutations in specific ASD risk genes[56]. This divergent pattern of cellular maturation is in line with human genetic studies that have repeatedly identified 22q11.2 deletions as top hits in studies of SCZ but not ASD genetic risk[57].

Transcriptomic analyses of key cell types further revealed that 22q11.2 deletions lead to pervasive and improperly orchestrated gene expression alterations in a wide range of cell types and ensembles of genes across the entire EN lineage. This analysis underscored biological pathways crucial for neuronal development and function that are affected by 22q11.2 deletions during human early brain development. Notably, in line with the well-established pleiotropy of the 22q11.2 deletions, gene expression alterations were also observed in a wide range of non-neuronal cell types, such as astrocytes and choroid plexus (**Supplemental Tables 2-5**). This suggests that 22q11. deletions may affect complementary aspects of the developmental program that are modulated by neuron/glia or neuron/CSF interactions. These findings need to be addressed in future studies.

Our analysis showed that miRNA dysregulation in patient organoids may alter, in a cell-type specific manner, both the level and the dynamic temporal profile of expression of genes involved in neuronal development and maturation. Aberrant levels and temporal regulation of

gene expression may impede both the onset and the unfolding of the maturation programs. This is consistent with a plethora of data supporting a role of miRNAs in regulating temporal transitions in gene expression throughout animal development[58-60] including human brain development[61]. Noteworthy targets of miRNA dysregulation include epigenetic regulators such as EZH2, a key component of a recently identified epigenetic barrier of maturation established before the onset of neurogenesis[54]. EZH2 was upregulated in early RG of DIV 70 patient organoids (*Padj* = 0.001, S**upplemental Table S2**). This raises the interesting possibility that the effects of miRNA dysregulation at this early stage may be mediated, at least in part, via the epigenetic machinery. Another noteworthy target is the *EMC10* gene, which shows altered temporal expression trajectory along the entire EN lineage at DIV70 and significant upregulation in patient RG (P = 1.56×10^{-6}), IPC-nEN (P = 5.3×10^{-5}) and EN (P = 7.3×10^{-6}) but not in astrocytes, choroid or interneuron lineage cells (**Supplemental Table S2**). Indeed effective knockdown to near WT levels of *EMC10* in patient iPSC-derived neurons leads to restoration of key morphological and functional EN alterations emerging due to 22q11.2 deletions[12]. Furthermore, normalization of *Emc10* levels in either developing or adult mouse brain rescues several 22q11.2 deletion associated behavioral deficits[12, 31], establishing a clear link between miRNA regulatory mechanisms and aspects of the behavioral manifestations observed in 22q11.2 deletion carriers.

While altered miRNA biogenesis may affect the pace at which neuronal development unfolds, it is likely that it is not the only driving factor. Results from both human genetic and animal model studies suggest that the deficits seen in the 22q11.2 deletion carriers are due to cumulative and concerted actions, along developmental time and space, of multiple resident genes within the deleted region[62,63,64]. This is supported by our PPI centrality analysis, which suggests that 22q11.2 genes, in addition to DGCR8, may have complementary contributions to the altered signaling pathways in distinct cell types and developmental stages. We identified *RANBP1, HIRA* and *CLTCL1* as key candidates underlying perturbations of protein networks at

the early radial glial stage. Similarly, HIRA and PI4KA were identified as key component of regulatory protein networks affected in embryonic EN. These results suggest that multiple level experiments are needed to understand the integrated contribution of deleted genes towards therapeutic interventions.

A distinctive feature of 22q11.2DS is that it represents one of the highest known genetic risk groups for SCZ. Previous studies have shown that SCZ risk genes targeted by rare *de novo* mutations often exhibit highest expression during the prenatal period[65]. Many prenatally-biased risk genes are highly expressed during the first and second trimester of pregnancy, a period of active cortical neurogenesis and a vulnerable time for brain development due to highly dynamic changes in gene expression, high level expression of genes intolerant to mutations and increased susceptibility to environmental insults[61,66,67]. Consistently, we have shown that genes carrying SCZ rare risk variants are enriched among DEGs in patient organoid neurons. This supports the notion that, for a fraction of patients with SCZ, genetic liability may affect the pace of early brain developmental trajectories similar to the ones described here. In that context, our findings may be generalized to other genetic causes of SCZ, especially ones with large effect mutations and have the potential to facilitate the pursuit of preventive and therapeutic interventions.

METHODS

hiPSC generation and characterization: Q5, Q6, Q1, and Q2 iPSC lines were generated at the Columbia Stem Cell Core via non-integrating Sendai virus-based reprogramming of monocytes from donors with 22q11.2DS and SCZ and healthy sibling controls. Demographic and clinical information on patients is provided in **Supplemental Table 9**. QR19, QR23, QR20 and QR27 lines were obtained from the NIMH Repository and Genomics Resource (http://www.nimhstemcells.org/)[68]. We confirmed that all iPSC lines maintain their stemness using RT-PCR and immunostaining for stem cell markers (NANOG, OCT4/SOX4, SSEA-4 and TRA-1–60[12] and genomic stability using G-band karyotype analysis. We confirmed the genotypes and the size of the 22q11.2 deletion using a multiplex ligation-dependent probe amplification (MLPA) assay[69].

Generation of dorsal forebrain cerebral organoids: We generated dorsal forebrain patterned organoids using a protocol that was adapted from Kadoshima et al[11]. At DIV 40, organoids were transferred to maintenance media containing 1% N2 and 2% FBS. After DIV 80, they were maintained in media containing 1% N2, 2% FBS and 1% B27 supplement.

Bulk RNA-seq: We used a set of patient and control organoids at DIV70 (8-10 organoids per line, 4 case and 4 control lines). The organoids were transduced with the AAV-hSYN-GFP virus two weeks before DIV70 (Addgene, 105539-AAV1). We dissociated the transduced organoids using papain digestion (Worthington, LK003160) and sorted the GFP positive neurons by FACS. Neurons were lysed in TRIzol reagent (Thermo Fisher Scientific, 15596026) and total RNA was extracted from the cells using Qiagen RNeasy Kit (Qiagen, 74104). Quality control checks using a Bioanalyzer (Agilent 2100 bioanalyzer) were performed to ensure the RNA Integrity Number (RIN)>9.0 for all samples. Library preparation and RNA sequencing were conducted to generate 20 million paired-end reads at the Columbia Genome Center on Illumina Novaseq 6000 instrument using STRYPOLYA library prep kit. Raw reads were processed and aligned to human genome (hg38) using the STAR alignment tool[70]and the

gene count matrix generated was analyzed using the DeSEQ2 pipeline to identify the DEGs[71]. The genes with LFC>0.2 and an adjusted P<0.05 were considered as DEGs in downstream analysis. GO term enrichment was performed using the G:Profiler tool[72]. The PPI network was analyzed using string-db (https://string-db.org).

miRNA-seq: Total RNA extraction with miRNA enrichment was performed using the Vana™ miRNA Isolation Kit (Thermo Fisher Scientific, AM1561). Total RNA quality and quantity was assayed with Bioanalyzer 2100 (Agilent, CA, USA), with RIN number >7.0. Approximately 1 g of total RNA was used to prepare small RNA library according to the protocol of TruSeq Small RNA Sample Prep Kits (Illumina, San Diego, CA, USA) and single-end sequencing 50bp on an Illumina Hiseq 2500 (following the vendor's recommended protocol) was conducted as described in ref. For the GO-term enrichment analysis of the target genes of differentially expressed miRNAs (153/133, DEmiRs), the webtool miRNet 2.0 (https://www.mirnet.ca/) with standard settings (tissue: all, targets: genes [TargetScan]) was used[73]. Analysis of the overlap of dysregulated genes and miRNA targets was performed by converting the gene lists to their corresponding genomic coordinates. To assess the significance of the overlap between gene sets, we extracted the genomic coordinates of all genes that were expressed in the organoids (determined by their expression levels in scRNA-seq) as the search space and used the randomization function in RegioneR to "resample" the regions that only contain the genes in the search space[74]. One randomly "resampled" region set had the same size as the dysregulated genes, while the other randomly "resampled" region set had the same size as miRNA targets. The number of overlaps between these two region sets was determined by RegioneR and 1000 permutations were performed to generate a frequency distribution of random overlaps between two region sets to determine the empirical p value of the actual overlaps.

scRNA-seq: We generated a high viability (>90%) single cell suspension from 3 pairs of 70-day old organoids, a total of 6 distinct lines with 3 organoids per line. The single cell suspension was sequenced on the 10x Genomics platform at the Columbia Genome Center.

Our analysis workflow included (i) aggregation with depth normalization[75] (ii) Quality Control[15] (iii) Normalization (Scran[76]), (iv) Integration (LIGER[77]), (v)Clustering (Leiden[16]), (vi) Differential Gene Expression Analysis (vii) Visualization (UMAP[78]) (viii) Cell type annotation (SingleR[18]). We used a recently published dataset that classified the signature transcriptomic profiles of the cell types within the human fetal forebrain at various stages of development[17], as a cell type signature reference to annotate the cells in our data. We used a custom-built stratified subsampling approach to validate cell type annotations and calculated the percentage of times a particular annotation is assigned to a cell over multiple random training permutations on stratified subsamples. Next, we defined high-confidence annotations as those that had a higher percentage than random assignments and ensured that 98% of our cell type annotations were high-confidence. We compared cell type distribution differences using scCODA[19]. We conducted an analysis of DEGs in various cell type populations using the MAST pipeline[24].

For WGCNA analysis of control organoids at DIV70, we converted the scRNA-seq dataset into Seurat format, subset cells in the excitatory neuron lineage and used the scWGCNA pipeline with default settings and using top 2000 variable genes for the analysis[26]. After the WGCNA modules were identified, we scored the expression of module genes in both patient and control datasets at DIV70 using the “scanpy.tl.score.genes” function and compared the expression scores of these WGCNA modules using a linear model with each individual iPSC line as random variable and genotype as a predictor as described previously[56].

To assess developmental trajectories, we employed two approaches. First, we used Monocle3 [79] to assess pseudotime trajectories of different developmental lineages in our scRNA-seq dataset. For each lineage and DIV, we plotted Ridgeline plots of cell distribution along pseudotime and performed the Kolmogorov-Smirnov test to assess if the distributions were significantly different between patient and control organoids[56]. Second, we used the scVelo tool [22] to analyze RNA velocity of individual cells in batch-corrected patient and control organoid datasets as a whole, followed by an analysis of differentiation potential and absorption

probability using the CellRank tool[21]. Latent time represents an internal clock of each cell based on its transcriptional dynamics and reveals the time a cell stays in the current status before it transits to the next cell fate status.

For analysis of transcription factor regulatory networks, we used the pYSCENIC pipeline[80]. First, we generated a representation of the DIV70 dataset in TF space and confirmed that our cell representation is consistent with cell-type annotation within this space. For example, we could detect enhanced activity of the neuronal transcription factors NEUROD1 in the neuronal clusters while the stem and progenitor cell marker SOX2 has a higher activity in the radial glia and cycling progenitor clusters. After we identified differentially active TF between patients and controls in various cell types, we compiled the top differentially active TF and their downstream effector genes (regulons) and conducted GO term enrichment analysis on the effector genes. GO term enrichment of DEGs obtained from the above analysis was performed using G:Profiler[72]

Analysis of cell proliferation: For FACS-based cell cycle analysis we dissociated organoids as described above, roughly equal number of dissociated cells per line were fixed in chilled 70% ethanol at 4°C for 1 hour. Cells were washed 2 times with PBS, 5ug of Ribonuclease 1 (Qiagen, 19101) was added to each sample followed by staining with 20ug propidium iodide (Thermo Scientific, P1304MP) and 0.1% Triton for 30 min prior to FACS. To assess the proliferation rate of dividing cells, organoids were treated with 0.02µm BrdU to label the cells in S-phase (Sigma Aldrich, B5002-100MG) in organoid culture medium for 2 hours, washed and then fixed as described above. Organoids were subjected to 3D immunostaining using a protocol modified from the iDISCO whole-mount staining protocol (https://idisco.info/idisco-protocol/) that allowed 3D imaging of a large area and depth (200µm) of the organoid. Samples were washed, permeabilized in 0.2% TritonX-100 for 24 hours at 37°C and blocked in 10% Horse serum and 0.2% TritonX-100 for 24h at 37°C. Primary antibodies were then added along with 10ug/ml Heparin, 3% Horse serum and 0.2% Tween-20 for 50

hours at 37°C. Primary antibodies used for cell cycle analyses were rat anti-BrdU (Abcam, ab6326, 1:300), rabbit anti- Ki67 (Abcam, ab15580, 1:200) and goat anti-SOX2 (R&D Systems, AF2018-SP, 1:200). Samples were then washed and treated with secondary antibodies (donkey secondary antibodies Jackson Immunoresearch) at 1:300 dilution for 36 hours. Samples were then incubated overnight with DAPI, washed and then mounted in RapiClear medium (SunJin Labs, RC149002) in 18 well chamber slides (Ibidi, 8187) overnight for clearing and imaging on W1-Yokogawa Spinning Disk Confocal (Nikon Instruments, Tokyo, Japan) at 40x magnification. To analyze the images, the DAPI channel was first segmented using ilastik[81] to provide a binary segmentation mask of the nucleus foreground from the background. Binary erosion of the DAPI mask was performed on Fiji[82] to remove noise points. The “distance transform watershed 3D” method from MorphoLibJ[83] on Fiji was used to extract and distinguish individual DAPI nuclei and assign them unique mask ID. Within the cell mask of each individual DAPI nucleus, the signal in other channels (BrDU, SOX2, Ki67) was measured using customized Python code and a cut-off threshold was applied to determine cell identity. The thresholds were manually chosen based on each image and were further proofread. Cell proportions were compared using the Kolmogorov-Smirnov test, $p<0.05$ was the significance threshold.

Analysis of neuronal morphology: We analyzed organoids at DIV70. At DIV55, we infected organoids for 2 weeks with the AAV1-hSYN-eGFP virus (Addgene, 105539-AAV1), which directs expression of eGFP under the neuron-specific synapsin promoter. At DIV67, we placed the organoids onto a glass coverslip and immobilized them in a droplet of 50% Matrigel in culture media (Corning, 354277). At DIV70, organoids were fixed in 4%PFA (Biotium, 22023) for 3h at RT and then blocked for 1.5h at RT in 0.3% Triton-X and 10% horse serum (catalog#H0146, Sigma-Aldrich, St. Louis, MO, USA) solution. After fixation, organoids were stained with the primary got anti-GFP antibody (Rockland, 600-101-215, 1:500) to amplify the fluorescence signal in a 0.1% Triton-X and 2% horse serum solution overnight at 4°C. Coverslips were then washed 3x15 min with DPBS (catalog#D8537, Sigma-Aldrich, St. Louis,

MO, USA) and cells were incubated for 2h with the secondary antibody at room temperature followed by 3x15 min DPBS washing. Organoids were imaged as a whole mount on W1-Yokogawa Spinning Disk Confocal (Nikon Instruments, Tokyo, Japan) at 40x magnification to facilitate imaging of a large area of the organoid without sectioning and thus preserving the cell morphology. We generated 3D traces of individual neurons using Imaris (Bitplane). We quantified the number of branchpoints, number of primary neurites and total neurite length for each traced cell. We analyzed a total of 8-11 organoids per line over 3-4 separate batches generated on different dates. A total of 66-166 cells per iPSC line were analyzed at DIV70. In addition to immunostaining for GFP, in a subset of organoids, we performed immunostaining for the somatodendritic marker MAP2 (chicken anti-MAP2, Abcam, ab5392, 1:500) and immature neuron marker DCX (mouse anti-DCX, Santa Cruz Biotech sc-271390, 1:250) to assess cell development and neurite specification.

Analysis of organoid growth: To analyze global organoid growth, organoids were imaged weekly using a bright field microscope (4x objective, Zeiss Primovert inverted microscope). Fiji[82] was used to trace the border of the organoids and define regions of interest (ROIs). For each time point, 2 parameters were measured; the perimeter of the ROI and the area enclosed by the ROI. These two measurements were used to track organoid size over time.

Ca^{2+} imaging: We constructed a novel Lentivirus vector driving GCAMP6s expression (Lenti-Ubi-mRuby2-GSG-p2A- GCAMP6s). Organoids were transduced with the Lentivirus vector 14 days prior to recording. Ca^{2+} activity as indicated by GCAMP6s fluorescence intensity was assessed visually prior to image acquisition. GCAMP6s signal was recorded for 25 min using an Olympus IX81 epifluorescence microscope at 4x magnification, with a frame rate of 1 frame per second (fps) and recorded for 1500 frames. At the 500 second mark, a glutamate solution was added to the culture medium at a final concentration of 100 μM. Ca^{2+} activity was measured in a set of organoids that had been cultured for days 90, 168, 238 and 259 to

determine optimal timepoint for Ca^{2+} activities. Images were stabilized with a stabilizer plugin in ImageJ. Denoising, segmentation and Ca^{2+} event detection were performed using a CaImAn-based pipeline[84]. Ca^{2+} activities with DF/F local maxima value higher than five times the standard deviation from baseline were classified as one firing event. For Ca^{2+} event peak heights, only cells with temporally non-overlapping and distinguishable Ca^{2+} events were used, and only the Ca^{2+} event in the middle in temporal order was used in cases when one cell has multiple Ca^{2+} events.

Analysis of the overlap between genes harboring rare LoF risk variants and EN lineage cell types: We used DNENRICH[85] for calculating the permutation-based significance of gene set enrichment among genes hit by *de novo* mutations accounting for potential confounding factors such as gene sizes and local trinucleotide contexts. DNENRICH analyses were performed using 100,000 permutations. The following inputs were used for this analysis: 1) gene name alias file: the default dataset included in the DNENRICH package, 2) gene size matrix file: the default dataset included in the DNENRICH package (for RefSeq genes), 3) gene set file: the set of DEGs identified by the MAST analysis of individual cell types; all genes were equally weighted, 4) mutation list files: lists of genes (equally weighted) carrying LoF DNMs in SCZ, ID/DD, NDD and ASD from denovo-db SSC and non-SSC. For SCZ we also added significant and nominally significant DNMs from the SCHEMA dataset ($p<0.05$, https://schema.broadinstitute.org/results) and 5) background gene file: the default gene list in the gene size matrix. The numbers of LoF DNMs in SCZ, ID/DD, ASD were 1657, 1373, 997 and the respective numbers of synonymous mutations were 3610, 794, 1644. For analyses restricting the input LoF DNMs to those in genes intolerant to LoF mutations, we used pLI scores≥0.9[42].

Protein-protein interaction (PPI) network analysis: We used the search tool for retrieval of interacting genes (STRING) (https://string-db.org) database, which integrates both known and predicted PPIs, to seek potential interactions between DEGs and visualize functional

interactions of these proteins. Active interaction sources, including text mining, experiments, databases, and co-expression as well as species limited to “Homo sapiens” and an interaction score > 0.4 were applied to construct the PPI networks. A centrality analysis on each PPI network was conducted to estimate how important a node or edge is for the connectivity or the information flow of the network using CINNA (Central Informative Nodes in Network Analysis)[86] R package.

Author Contributions: B.X., J.A.G. and S.B.R. contributed to the conception and design of the study; B.X. and J.A.G. supervised all the analyses; S.B.R., H.Z. and Y.S. contributed to characterization and maintenance of human iPSC line as well as generation and culture of organoids; R.J.S contributed to the collection and clinical diagnosis of patients; S.M. contributed to the clinical characterization of patients and the generation of iPSC lines; S.B.R., F.B., R.R., B.X. contributed to scRNAseq data analysis; S.B.R, Y.C, R.T, B.X., Y.S, H.Z. contributed to calcium imaging and cell proliferation imaging analysis; S.B.R, Y.S. and H.Z. contributed to dendritic morphology analysis; K.W.L. supervised the optimization of the organoid culture conditions; S.B.R., B.X. and J.A.G prepared the manuscript with contributions from all co-authors.

Acknowledgements

We thank Barbara Corneo and the Columbia Stem Cell Core Facility for the Q1, Q2, Q5 and Q6 hiPSC lines generation. Bio- samples of Q20 and Q27 hiPSCs were obtained from NIMH Repository & Genomics Resource. We thank Linda Brzustowicz and Bill Manley from the Rutgers University and the staff members at RUCDR. Data and biomaterials generated in Study 125/Site 393 were funded by a NIMH grant to Dr. Herb Lachman (MH087840: Analysis of Glutamatergic Neurons Derived from Patient- Specific iPS Cells). The co-investigators on this grant included Dr. Deyou Zheng and Dr. Reed Carroll from the Albert Einstein College of

Medicine. Patients and controls were recruited at the Albert Einstein College of Medicine and at the Child Psychiatry Branch, NIMH, directed by Dr. Judith L. Rapoport. We thank all participating subjects and their families for their contributions. This work was supported by National Institute of Health-NCATS grant (UG3/UH3TR002151) and National Institute of Mental Health Grant (2R01MH097879). We thank the Zuckerman Institute Cellular Imaging core for support with imaging and analysis pipelines for 3D imaging of the organoids and the Zuckerman Institute Flow Cytometry Core for support for FACs sorting. We thank Columbia University Genome Center for support with bulk and scRNAseq execution. We thank Anqi Wang and other members in the Rabadan lab for support with cloud computing and data storage, as well as advice on scRNAseq data analysis. We thank Khakima Khalizova for her help in preparing the figures.

Competing interests

The authors declare that they have no conflict of interest.

Data availability

The raw sequencing data described in this manuscript have been deposited into the NIH Gene Expression Omnibus (GEO) database under accession number GSE244010 and are available at the following URL: https://www.ncbi.nlm.nih.gov/geo/query/acc.cgi?acc= GSE244010.

Figure Legends

Fig 1: Organoid growth and neuronal activity analysis. (a) Box plots depicting increase in organoid surface area in patient and control organoids at different time points normalized to week 1. **(b)** Box plots depicting increase in organoid perimeter in patient and control organoids at different time points normalized to week 1. **(c)** Representative denoised and segmented epifluorescence microscope images (4x) of Ca^{2+} unit signals detected in organoids *in situ* **(d)** Average peak-aligned traces (DF/F vs time, zero corresponding to peak time) of Ca^{2+} transients detected in different units (cells) in patient (red) and control (black) organoids. Three patient and three control organoids from two independent batches analyzed at this timepoint (average number of cells per organoid: n for patient = 89, n for control = 124). *Left:* Combined aligned traces from batches 1 and 2, *Middle:* Batch 1, *Right:* Batch 2. **(e)** Quantification of Ca^{2+} peak amplitude in patient (red) and control (black) organoids. Patient organoids show significantly lower peak amplitude. *Left:* Combined batches 1 and 2 (Kolmogorov-Smirnov test, $P = 5.78 \times 10^{-12}$), *middle:* Batch 1 (Kolmogorov-Smirnov test, $P = 3.90 \times 10^{-3}$), *right:* Batch 2 (Kolmogorov-Smirnov test, $P = 3.77 \times 10^{-10}$).

Fig 2: Cell type composition and proliferation analysis of organoids.

(a) *Left*: Annotation of cell types in the dataset with reference to human fetal brain[17]. Most of cell types in the developing human brain are successfully recapitulated. *Right*: UMAP color-coded to highlight distribution of annotated cell types in DIV70 (blue) and DIV150 (orange). **(b)** Density maps depicting the relative spatial allocation of cells in control (*left*) and patient (*right*) organoids at DIV70. There is a higher cell density in progenitor regions and lower cell density in differentiated neuron regions in patient organoids compared to control. **(c)** Quantification of relative numbers of major cell types in control (grey) and patient organoids (red) at DIV70. A significantly lower fraction of neurons is observed at DIV70 in patient organoids. **(d)** Representative confocal microscope images (40x) of a single 2D Z-stack of control (*top*) and

patient (*bottom*) organoid whole-mount preparations stained for cell cycle markers and BrdU. Depicted are DIV70 organoids double labelled for NPC marker SOX2 and nuclear marker DAPI (*left*), NPC marker SOX2 and active cell cycle marker Ki67 (*middle*) and NPC marker SOX2 and S phase marker BrdU (*right*). Scale bar = 20µm. **(e, f)** Quantification of the fraction of cells labelled with the aforementioned markers reveals that the fraction of active cycling progenitors is significantly higher in patient organoids. **(e)** Quantification of cell cycle markers in patient and control organoids (n for patient = 12, n for control = 13, from 3 independent batches). *Left:* Total number of SOX2 positive NPCs as percentage of DAPI-labeled cells. *Middle*: Fraction of active cycling (Ki67-positive) NPCs (SOX2-positive) (Kolmogorov-Smirnov test, P = 0.04). *Right*: Fraction of S-phase (BrdU-positive) NPCs (SOX2 positive). **(f)** Quantification of cell cycle markers per ROI (26-34 ROIs per line) in individual patient-control pairs. *Left*: Number of SOX2-positive NPCs represented as percentage of DAPI-labelled nuclei (Kolmogorov-Smirnov test, P = 0.01). *Middle*: Fraction of active cycling (Ki67-positive) NPCs (SOX2-positive) (Kolmogorov-Smirnov test, P_{pair1} = 0.25, P_{pair2} = 0.01, P_{pair3} = 5.78×10^{-5}). *Right*: Fraction of S-phase (BrdU-positive) NPCs (SOX2-positive) (Kolmogorov-Smirnov test, P_{pair1} = 0.4 P_{pair2} = 0.003, P_{pair3} = 0.0004).

Fig 3: Pseudotime analyses of the pace of neuronal development.

(a) Pseudotime trajectory at DIV70 colored by pseudotime. **(b)** Ridge plot depicting distribution of cells in patient and control EN lineage at DIV70. Patient cell distribution is shifted towards early points of the trajectory represented by progenitors while control cell distribution is more dispersed. There is a significant difference between the two distributions (Kolmogorov-Smirnov test, P = 1.33×10^{-11}). **(c)** RNA velocity embedding stream at DIV70 depicting the EN lineage trajectory in control (*left*) and patient (*right*) organoids. **(d)** UMAP plots colored by differentiation potential in control (*left*) and patient (*right*) DIV70 EN lineage. Progenitors in control organoids

show high differentiation potential while progenitors in patient organoids show low differentiation potential.

(e) Pseudotime trajectory at DIV150 colored by pseudotime. **(f)** Ridge plot showing distribution of cells in patient and control DIV150 EN lineage. Patient cell distribution is largely shifted to early points of the trajectory represented by more immature stages of the lineage while control cell distribution is shifted towards later points along the pseudotime. There is a significant difference between the two distribution (Kolmogorov-Smirnov test, $P = 2.13 \times 10^{-4}$). **(g)** Pseudotime trajectory of cells in patient and control IN lineage colored by pseudotime. **(h)** Ridge plot depicting distribution of cells in patient and control IN lineage along pseudotime. Patient cell distribution is shifted towards early points along pseudotime while control cell distribution is more dispersed. There is a significant difference between the two distributions (Kolmogorov-Smirnov test, $P = 1.33 \times 10^{-2}$). **(i)** Pseudotime trajectory of progenitor populations generated with Monocle2. Trajectory starts at cyc-RG and cyc-IPC and progresses to RG-early. Later pseudotimes are represented by RG-late and IN progenitors such as MGE-RG, MGE-IPC and MGE-RG-IPC-DIV. **(j)** Ridge plot depicting distribution of progenitors in patient and control lineage Patient cell distribution is shifted largely to early points of the trajectory represented by earlier progenitors while control cell distribution is shifted more towards later time points. There is a significant difference between the two distribution (Kolmogorov-Smirnov test, $P = 4.53 \times 10^{-6}$), indicating a developmental delay at the level of the progenitors.

Fig 4: Morphological and transcriptional signatures of impaired EN maturation.

(a) Representative 3D traces of neurons generated from confocal images of DIV70 cultures of control (*left*) and patient (*right*) organoids. **(b)** Quantification of combined patient and control number of primary neurites per cell (*left*), total neurite length (*middle*) and number of branchpoints per cell (*right*) across multiple experiments (unpaired t-test, $P < 0.05$). 8-11

organoids were analyzed per line over 3-4 batches for a total of 66-166 cells for each line. Data are presented as mean ± SD, each point represents averaged data from a unique line and batch. **(c)** Quantification of number of primary neurites per cell (*left*), total neurite length (*middle*) and number of branchpoints per cell (*right*) for different patient and control paired organoids. Data are presented as mean ± SD. Across all pairs, patient neurons have a significantly simpler neurite architecture (Mann Whitney Test, $P < 0.05$). Neurons analyzed with immunostaining were positive for MAP2 and immature neuron marker DCX (see also **Fig S1b**, *bottom*). **(d)** Volcano plot showing differentially expressed genes in sorted neurons from DIV70 patient organoids compared to control. **(e,f)** GO term enrichment analysis of top downregulated **(e)** and upregulated **(f)** DEGs in patient neurons. **(g)** SynGO gene enrichment analysis of genes downregulated (*left*) and upregulated (*right*) in patient neurons. There is a significant enrichment of synaptic genes among the downregulated genes ($P = 0.00005$), with a particular enrichment for transcripts with presynaptic/synaptic vesicle functions (GO:0045202/GO:0098793, $P = 0.0331$), but no significant enrichment of synaptic genes among upregulated genes.

Fig 5: Gene modules and functions dysregulated in the EN lineage of patient organoids. **(a)** Volcano plot showing DEGs identified in patient cyc-RG compared to control. **(b)** GO term enrichment analysis of DEGs in patient cyc-RG. Cell cycle and proliferation genes are upregulated while neurogenic genes are downregulated. **(c)** Volcano plot showing DEGs identified in patient ENs compared to control. **(d)** GO term enrichment analysis of DEGs in patient ENs. Genes related to negative regulation of neurogenesis are upregulated while genes related to promotion of neurogenesis are downregulated. **(e)** UMAP of cell clusters in EN lineage cells in control organoids. **(f)** Identification of clusters of co-expressed genes using scWGCNA in control EN lineage cells. From *left* to *right*: Modules 2 and 9 are expressed in cycling progenitors and progenitor cells respectively and modules 3 and 4 are expressed in EN clusters. **(g)** Scanpy scoring of module genes identified in **(e)** and **(f)** in control and patient EN

lineage cells. Expression of modules 2 and 9 are significantly lower (module 2, P = 0.002591; module 9, P = 0.03008) in control compared to patient cells.

Fig 6: 22q11.2-associated genes and genetic pathways underlying altered developmental pace. (a) Volcano plot depicting differentially expressed miRNAs in whole patient organoids at DIV70. **(b)** mirNet analysis of the network of downregulated miRNAs in patient organoids **(c)** GO term enrichment of mirNet-T computed targets of downregulated miRNAs. Targets are enriched for nuclear genes associated with cell cycle and cell division. **(d)** Latent time analysis of a subset of putative target genes of downregulated miRNAs using scVelo and CellRank; y axis denotes expression level; x axis denotes latent time. **(e)** PPI network analysis of dysregulated genes in patient cyc-RG (*left*) and ENs (*right*) with scoring of the contributions of the 22q11.2 locus genes to the network.

Fig 7: Overlap between genes harboring rare LoF risk variants and EN lineage cell types. Results from permutation-based analysis of overlap between EN lineage cell types and DEGs harboring rare coding damaging variants at DIV70 (*top*) and DIV150 (*bottom*) using the DNENRICH pipeline and curated reference datasets. Overlap between cell types in the EN lineage and dysregulated genes harboring LoF risk variants **(a)**, highly intolerant LoF variants (pLI ≥ 0.9) **(b),** or synonymous variants **(c).**

References

1 Morrison, S. *et al.* Cognitive deficits in childhood, adolescence and adulthood in 22q11.2 deletion syndrome and association with psychopathology. *Transl Psychiatry* **10**, 53, doi:10.1038/s41398-020-0736-7 (2020).

2 Woodin, M. *et al.* Neuropsychological profile of children and adolescents with the 22q11.2 microdeletion. *Genet Med* **3**, 34-39, doi:10.1097/00125817-200101000-00008 (2001).

3 Xu, B. *et al.* Strong association of de novo copy number mutations with sporadic schizophrenia. *Nat Genet* **40**, 880-885, doi:10.1038/ng.162 (2008).

4 Birchwood, M., McGorry, P. & Jackson, H. Early intervention in schizophrenia. *Br J Psychiatry* **170**, 2-5, doi:10.1192/bjp.170.1.2 (1997).

5 Lewis, D. A. & Levitt, P. Schizophrenia as a disorder of neurodevelopment. *Annu Rev Neurosci* **25**, 409-432, doi:10.1146/annurev.neuro.25.112701.142754 (2002).

6 Rapoport, J. L., Addington, A. M., Frangou, S. & Psych, M. R. The neurodevelopmental model of schizophrenia: update 2005. *Mol Psychiatry* **10**, 434-449, doi:10.1038/sj.mp.4001642 (2005).

7 Pantelis, C. *et al.* Neuroanatomical abnormalities before and after onset of psychosis: a cross-sectional and longitudinal MRI comparison. *Lancet* **361**, 281-288, doi:10.1016/S0140-6736(03)12323-9 (2003).

8 Di Lullo, E. & Kriegstein, A. R. The use of brain organoids to investigate neural development and disease. *Nat Rev Neurosci* **18**, 573-584, doi:10.1038/nrn.2017.107 (2017).

9 Chiaradia, I. & Lancaster, M. A. Brain organoids for the study of human neurobiology at the interface of in vitro and in vivo. *Nat Neurosci* **23**, 1496-1508, doi:10.1038/s41593-020-00730-3 (2020).

10 Velasco, S., Paulsen, B. & Arlotta, P. 3D Brain Organoids: Studying Brain Development and Disease Outside the Embryo. *Annu Rev Neurosci* **43**, 375-389, doi:10.1146/annurev-neuro-070918-050154 (2020).

11 Kadoshima, T. *et al.* Self-organization of axial polarity, inside-out layer pattern, and species-specific progenitor dynamics in human ES cell-derived neocortex. *Proc Natl Acad Sci U S A* **110**, 20284-20289, doi:10.1073/pnas.1315710110 (2013).

12 Thakur, P. L., Martin; Diamantopoulou, Anastasia ; Rao, Sneha; Chen,Yijing; Ferng, Annie; Mazur, Curt; Kordasiewicz, Holly; Shprintzen, Robert J; Markx, Sander ; Xu, Bin; Gogos, Joseph A. EMC10 reduction in human neurons and adult mouse brain rescues cellular and behavioral deficits linked to 22q11. 2 deletion. *biorxiv* (2021).

13 Khan, T. A. *et al.* Neuronal defects in a human cellular model of 22q11.2 deletion syndrome. *Nat Med* **26**, 1888-1898, doi:10.1038/s41591-020-1043-9 (2020).

14 Sun, Z., Williams, D. J., Xu, B. & Gogos, J. A. Altered function and maturation of primary cortical neurons from a 22q11.2 deletion mouse model of schizophrenia. *Transl Psychiatry* **8**, 85, doi:10.1038/s41398-018-0132-8 (2018).

15 Ilicic, T. *et al.* Classification of low quality cells from single-cell RNA-seq data. *Genome Biol* **17**, 29, doi:10.1186/s13059-016-0888-1 (2016).

16 Traag, V. A., Waltman, L. & van Eck, N. J. From Louvain to Leiden: guaranteeing well-connected communities. *Sci Rep* **9**, 5233, doi:10.1038/s41598-019-41695-z (2019).

17 Nowakowski, T. J. *et al.* Spatiotemporal gene expression trajectories reveal developmental hierarchies of the human cortex. *Science* **358**, 1318-1323, doi:10.1126/science.aap8809 (2017).

18 Aran, D. *et al.* Reference-based analysis of lung single-cell sequencing reveals a transitional profibrotic macrophage. *Nat Immunol* **20**, 163-172, doi:10.1038/s41590-018-0276-y (2019).

19 Buttner, M., Ostner, J., Muller, C. L., Theis, F. J. & Schubert, B. scCODA is a Bayesian model for compositional single-cell data analysis. *Nat Commun* **12**, 6876, doi:10.1038/s41467-021-27150-6 (2021).
20 Qiu, X. *et al.* Reversed graph embedding resolves complex single-cell trajectories. *Nat Methods* **14**, 979-982, doi:10.1038/nmeth.4402 (2017).
21 Lange, M. *et al.* CellRank for directed single-cell fate mapping. *Nat Methods* **19**, 159-170, doi:10.1038/s41592-021-01346-6 (2022).
22 Bergen, V., Lange, M., Peidli, S., Wolf, F. A. & Theis, F. J. Generalizing RNA velocity to transient cell states through dynamical modeling. *Nat Biotechnol* **38**, 1408-1414, doi:10.1038/s41587-020-0591-3 (2020).
23 Koopmans, F. *et al.* SynGO: An Evidence-Based, Expert-Curated Knowledge Base for the Synapse. *Neuron* **103**, 217-234 e214, doi:10.1016/j.neuron.2019.05.002 (2019).
24 Finak, G. *et al.* MAST: a flexible statistical framework for assessing transcriptional changes and characterizing heterogeneity in single-cell RNA sequencing data. *Genome Biol* **16**, 278, doi:10.1186/s13059-015-0844-5 (2015).
25 Aibar, S. *et al.* SCENIC: single-cell regulatory network inference and clustering. *Nat Methods* **14**, 1083-1086, doi:10.1038/nmeth.4463 (2017).
26 Feregrino, C. & Tschopp, P. Assessing evolutionary and developmental transcriptome dynamics in homologous cell types. *Dev Dyn*, doi:10.1002/dvdy.384 (2021).
27 Fenelon, K. *et al.* Deficiency of Dgcr8, a gene disrupted by the 22q11.2 microdeletion, results in altered short-term plasticity in the prefrontal cortex. *Proc Natl Acad Sci U S A* **108**, 4447-4452, doi:10.1073/pnas.1101219108 (2011).
28 Stark, K. L. *et al.* Altered brain microRNA biogenesis contributes to phenotypic deficits in a 22q11-deletion mouse model. *Nat Genet* **40**, 751-760, doi:10.1038/ng.138 (2008).
29 Xu, B., Hsu, P. K., Stark, K. L., Karayiorgou, M. & Gogos, J. A. Derepression of a neuronal inhibitor due to miRNA dysregulation in a schizophrenia-related microdeletion. *Cell* **152**, 262-275, doi:10.1016/j.cell.2012.11.052 (2013).
30 Chang, L., Zhou, G., Soufan, O. & Xia, J. miRNet 2.0: network-based visual analytics for miRNA functional analysis and systems biology. *Nucleic Acids Res* **48**, W244-W251, doi:10.1093/nar/gkaa467 (2020).
31 Diamantopoulou, A. *et al.* Loss-of-function mutation in Mirta22/Emc10 rescues specific schizophrenia-related phenotypes in a mouse model of the 22q11.2 deletion. *Proc Natl Acad Sci U S A* **114**, E6127-E6136, doi:10.1073/pnas.1615719114 (2017).
32 Besson, V. *et al.* PW1 gene/paternally expressed gene 3 (PW1/Peg3) identifies multiple adult stem and progenitor cell populations. *Proc Natl Acad Sci U S A* **108**, 11470-11475, doi:10.1073/pnas.1103873108 (2011).
33 Kuwahara, A. *et al.* Tcf3 represses Wnt-beta-catenin signaling and maintains neural stem cell population during neocortical development. *PLoS One* **9**, e94408, doi:10.1371/journal.pone.0094408 (2014).
34 Gribble, S. L., Kim, H. S., Bonner, J., Wang, X. & Dorsky, R. I. Tcf3 inhibits spinal cord neurogenesis by regulating sox4a expression. *Development* **136**, 781-789, doi:10.1242/dev.027995 (2009).
35 Hoshiba, Y. *et al.* Sox11 Balances Dendritic Morphogenesis with Neuronal Migration in the Developing Cerebral Cortex. *J Neurosci* **36**, 5775-5784, doi:10.1523/JNEUROSCI.3250-15.2016 (2016).
36 D'Rozario, M. *et al.* Type I bHLH Proteins Daughterless and Tcf4 Restrict Neurite Branching and Synapse Formation by Repressing Neurexin in Postmitotic Neurons. *Cell Rep* **15**, 386-397, doi:10.1016/j.celrep.2016.03.034 (2016).

37 Szklarczyk, D. *et al.* The STRING database in 2023: protein-protein association networks and functional enrichment analyses for any sequenced genome of interest. *Nucleic Acids Res* **51**, D638-D646, doi:10.1093/nar/gkac1000 (2023).
38 Mencarelli, C. *et al.* RanBP1 Couples Nuclear Export and Golgi Regulation through LKB1 to Promote Cortical Neuron Polarity. *Cell Rep* **24**, 2529-2539 e2524, doi:10.1016/j.celrep.2018.07.107 (2018).
39 Li, Y. & Jiao, J. Histone chaperone HIRA regulates neural progenitor cell proliferation and neurogenesis via beta-catenin. *J Cell Biol* **216**, 1975-1992, doi:10.1083/jcb.201610014 (2017).
40 Bojjireddy, N. *et al.* Pharmacological and genetic targeting of the PI4KA enzyme reveals its important role in maintaining plasma membrane phosphatidylinositol 4-phosphate and phosphatidylinositol 4,5-bisphosphate levels. *J Biol Chem* **289**, 6120-6132, doi:10.1074/jbc.M113.531426 (2014).
41 Thapar, A. & Riglin, L. The importance of a developmental perspective in Psychiatry: what do recent genetic-epidemiological findings show? *Mol Psychiatry* **25**, 1631-1639, doi:10.1038/s41380-020-0648-1 (2020).
42 Lek, M. *et al.* Analysis of protein-coding genetic variation in 60,706 humans. *Nature* **536**, 285-291, doi:10.1038/nature19057 (2016).
43 Velasco, S. *et al.* Individual brain organoids reproducibly form cell diversity of the human cerebral cortex. *Nature* **570**, 523-527, doi:10.1038/s41586-019-1289-x (2019).
44 Gudbrandsen, M. *et al.* Brain morphometry in 22q11.2 deletion syndrome: an exploration of differences in cortical thickness, surface area, and their contribution to cortical volume. *Sci Rep* **10**, 18845, doi:10.1038/s41598-020-75811-1 (2020).
45 Lin, A. *et al.* Mapping 22q11.2 Gene Dosage Effects on Brain Morphometry. *J Neurosci* **37**, 6183-6199, doi:10.1523/JNEUROSCI.3759-16.2017 (2017).
46 Sun, D. *et al.* Large-scale mapping of cortical alterations in 22q11.2 deletion syndrome: Convergence with idiopathic psychosis and effects of deletion size. *Mol Psychiatry* **25**, 1822-1834, doi:10.1038/s41380-018-0078-5 (2020).
47 Bagautdinova, J. *et al.* Altered cortical thickness development in 22q11.2 deletion syndrome and association with psychotic symptoms. *Mol Psychiatry* **26**, 7671-7678, doi:10.1038/s41380-021-01209-8 (2021).
48 Ching, C. R. K. *et al.* Mapping Subcortical Brain Alterations in 22q11.2 Deletion Syndrome: Effects of Deletion Size and Convergence With Idiopathic Neuropsychiatric Illness. *Am J Psychiatry* **177**, 589-600, doi:10.1176/appi.ajp.2019.19060583 (2020).
49 Kriegstein, A., Noctor, S. & Martinez-Cerdeno, V. Patterns of neural stem and progenitor cell division may underlie evolutionary cortical expansion. *Nat Rev Neurosci* **7**, 883-890, doi:10.1038/nrn2008 (2006).
50 Lukaszewicz, A. *et al.* The concerted modulation of proliferation and migration contributes to the specification of the cytoarchitecture and dimensions of cortical areas. *Cereb Cortex* **16 Suppl 1**, i26-34, doi:10.1093/cercor/bhk011 (2006).
51 Takahashi, T., Goto, T., Miyama, S., Nowakowski, R. S. & Caviness, V. S., Jr. Sequence of neuron origin and neocortical laminar fate: relation to cell cycle of origin in the developing murine cerebral wall. *J Neurosci* **19**, 10357-10371, doi:10.1523/JNEUROSCI.19-23-10357.1999 (1999).
52 Garcia, K. E., Kroenke, C. D. & Bayly, P. V. Mechanics of cortical folding: stress, growth and stability. *Philos Trans R Soc Lond B Biol Sci* **373**, doi:10.1098/rstb.2017.0321 (2018).
53 Fish, J. L., Dehay, C., Kennedy, H. & Huttner, W. B. Making bigger brains-the evolution of neural-progenitor-cell division. *J Cell Sci* **121**, 2783-2793, doi:10.1242/jcs.023465 (2008).
54 Ciceri, G. *et al.* An epigenetic barrier sets the timing of human neuronal maturation. *bioRxiv*, 2022.2006.2002.490114, doi:10.1101/2022.06.02.490114 (2022).

55 Sebastian, R., Song, Y. & Pak, C. Probing the molecular and cellular pathological mechanisms of schizophrenia using human induced pluripotent stem cell models. *Schizophr Res*, doi:10.1016/j.schres.2022.06.028 (2022).
56 Paulsen, B. *et al.* Autism genes converge on asynchronous development of shared neuron classes. *Nature* **602**, 268-273, doi:10.1038/s41586-021-04358-6 (2022).
57 Marshall, C. R. *et al.* Contribution of copy number variants to schizophrenia from a genome-wide study of 41,321 subjects. *Nat Genet* **49**, 27-35, doi:10.1038/ng.3725 (2017).
58 Ambros, V. MicroRNAs and developmental timing. *Curr Opin Genet Dev* **21**, 511-517, doi:10.1016/j.gde.2011.04.003 (2011).
59 Pasquinelli, A. E. & Ruvkun, G. Control of developmental timing by micrornas and their targets. *Annu Rev Cell Dev Biol* **18**, 495-513, doi:10.1146/annurev.cellbio.18.012502.105832 (2002).
60 La Torre, A., Georgi, S. & Reh, T. A. Conserved microRNA pathway regulates developmental timing of retinal neurogenesis. *Proc Natl Acad Sci U S A* **110**, E2362-2370, doi:10.1073/pnas.1301837110 (2013).
61 Colantuoni, C. *et al.* Temporal dynamics and genetic control of transcription in the human prefrontal cortex. *Nature* **478**, 519-523, doi:10.1038/nature10524 (2011).
62 Karayiorgou, M., Simon, T. J. & Gogos, J. A. 22q11.2 microdeletions: linking DNA structural variation to brain dysfunction and schizophrenia. *Nat Rev Neurosci* **11**, 402-416, doi:10.1038/nrn2841 (2010).
63 Jensen, M. & Girirajan, S. An interaction-based model for neuropsychiatric features of copy-number variants. *PLoS Genet* **15**, e1007879, doi:10.1371/journal.pgen.1007879 (2019).
64 Sanders, S. J. *et al.* Insights into Autism Spectrum Disorder Genomic Architecture and Biology from 71 Risk Loci. *Neuron* **87**, 1215-1233, doi:10.1016/j.neuron.2015.09.016 (2015).
65 Xu, B. *et al.* Exome sequencing supports a de novo mutational paradigm for schizophrenia. *Nat Genet* **43**, 864-868, doi:10.1038/ng.902 (2011).
66 Shohat, S., Ben-David, E. & Shifman, S. Varying Intolerance of Gene Pathways to Mutational Classes Explain Genetic Convergence across Neuropsychiatric Disorders. *Cell Rep* **18**, 2217-2227, doi:10.1016/j.celrep.2017.02.007 (2017).
67 Selemon, L. D. & Zecevic, N. Schizophrenia: a tale of two critical periods for prefrontal cortical development. *Transl Psychiatry* **5**, e623, doi:10.1038/tp.2015.115 (2015).
68 Lin, M. *et al.* Integrative transcriptome network analysis of iPSC-derived neurons from schizophrenia and schizoaffective disorder patients with 22q11.2 deletion. *BMC Syst Biol* **10**, 105, doi:10.1186/s12918-016-0366-0 (2016).
69 Li, Y. *et al.* Investigation of Neurodevelopmental Deficits of 22 q11.2 Deletion Syndrome with a Patient-iPSC-Derived Blood-Brain Barrier Model. *Cells* **10**, doi:10.3390/cells10102576 (2021).
70 Dobin, A. *et al.* STAR: ultrafast universal RNA-seq aligner. *Bioinformatics* **29**, 15-21, doi:10.1093/bioinformatics/bts635 (2013).
71 Love, M. I., Huber, W. & Anders, S. Moderated estimation of fold change and dispersion for RNA-seq data with DESeq2. *Genome Biol* **15**, 550, doi:10.1186/s13059-014-0550-8 (2014).
72 Raudvere, U. *et al.* g:Profiler: a web server for functional enrichment analysis and conversions of gene lists (2019 update). *Nucleic Acids Res* **47**, W191-W198, doi:10.1093/nar/gkz369 (2019).
73 Fan, Y. *et al.* miRNet - dissecting miRNA-target interactions and functional associations through network-based visual analysis. *Nucleic Acids Res* **44**, W135-141, doi:10.1093/nar/gkw288 (2016).
74 Gel, B. *et al.* regioneR: an R/Bioconductor package for the association analysis of genomic regions based on permutation tests. *Bioinformatics* **32**, 289-291, doi:10.1093/bioinformatics/btv562 (2016).
75 Zheng, G. X. *et al.* Massively parallel digital transcriptional profiling of single cells. *Nat Commun* **8**, 14049, doi:10.1038/ncomms14049 (2017).

76 Lun, A. T., Bach, K. & Marioni, J. C. Pooling across cells to normalize single-cell RNA sequencing data with many zero counts. *Genome Biol* **17**, 75, doi:10.1186/s13059-016-0947-7 (2016).
77 Welch, J. D. *et al.* Single-Cell Multi-omic Integration Compares and Contrasts Features of Brain Cell Identity. *Cell* **177**, 1873-1887 e1817, doi:10.1016/j.cell.2019.05.006 (2019).
78 Becht, E. *et al.* Dimensionality reduction for visualizing single-cell data using UMAP. *Nat Biotechnol*, doi:10.1038/nbt.4314 (2018).
79 Trapnell, C. *et al.* The dynamics and regulators of cell fate decisions are revealed by pseudotemporal ordering of single cells. *Nat Biotechnol* **32**, 381-386, doi:10.1038/nbt.2859 (2014).
80 Van de Sande, B. *et al.* A scalable SCENIC workflow for single-cell gene regulatory network analysis. *Nat Protoc* **15**, 2247-2276, doi:10.1038/s41596-020-0336-2 (2020).
81 Berg, S. *et al.* ilastik: interactive machine learning for (bio)image analysis. *Nat Methods* **16**, 1226-1232, doi:10.1038/s41592-019-0582-9 (2019).
82 Schindelin, J. *et al.* Fiji: an open-source platform for biological-image analysis. *Nat Methods* **9**, 676-682, doi:10.1038/nmeth.2019 (2012).
83 Legland, D., Arganda-Carreras, I. & Andrey, P. MorphoLibJ: integrated library and plugins for mathematical morphology with ImageJ. *Bioinformatics* **32**, 3532-3534, doi:10.1093/bioinformatics/btw413 (2016).
84 Giovannucci, A. *et al.* CalmAn an open source tool for scalable calcium imaging data analysis. *Elife* **8**, doi:10.7554/eLife.38173 (2019).
85 Fromer, M. *et al.* Gene expression elucidates functional impact of polygenic risk for schizophrenia. *Nat Neurosci* **19**, 1442-1453, doi:10.1038/nn.4399 (2016).
86 Ashtiani, M., Mirzaie, M. & Jafari, M. CINNA: an R/CRAN package to decipher Central Informative Nodes in Network Analysis. *Bioinformatics* **35**, 1436-1437, doi:10.1093/bioinformatics/bty819 (2019).
87 Liberzon, A. *et al.* The Molecular Signatures Database (MSigDB) hallmark gene set collection. *Cell Syst* **1**, 417-425, doi:10.1016/j.cels.2015.12.004 (2015).

SUPPLEMENTARY INFORMATION

Supplementary Figure Legends

Fig S1: Cell type composition of cultured organoids. Representative confocal images (40x) of 30µm sections from DIV70 organoids immunohistochemically labelled for cell type specific and cell cycle markers: (**a)**. Cell-type specific markers for neural progenitors (PAX6, FOXG1, PH3) and neurons (CTIP2, TBR1 and SATB2). Scale bar = 100µm. (**b).** Cell-type specific markers for radial glia (Nestin, *top*) intermediate progenitor cells (TBR2, *middle*) and proliferating/cycling cells (PH3/Ki67, *bottom*). Neurons are labeled with AAV1-hSYN1-GFP. Scale bar = 50 µm **(c)** Immunofluorescence staining for somatodendritic marker MAP2 (left) and immature neuron marker doublecortin (DCX) (*right*). Scale bar = 20µm

Fig S2: Quality control and clustering metrics of scRNA-seq data. (a) Distribution of total number of genes (*top*), mitochondrial transcripts (*middle*) and ribosomal transcripts (*bottom*) per sample. Quality control metrics are uniform across organoids from all iPSC lines. **(b, c)** Expression of genes related to hypoxia and apoptosis curated in the GSEA Hallmark mSigDB database[87]. There is no difference in expression of apoptosis or hypoxia-related genes between patient and control organoids as well as between DIV70 and DIV150 organoids. **(d)** Spatial representation of 8 transcriptomically distinct clusters (*left*) and distribution of clusters in individual samples (*right*). All samples show a similar distribution of clusters. **(e)** Dot-plot depicting expression of 22q11.2 locus genes in scRNA-seq datasets from patient and control organoid. **(f)** Expression of 22q11.2 locus genes across all samples. Analysis confirmed the expected ~50% decrease in patient relative to control organoids and demonstrated that they faithfully recapitulate the expected 22q11.2 locus gene expression profile with high organoid-to-organoid reproducibility.

Fig S3: Relative proportion of cell types in control organoids.

Stacked bar plots depicting the relative proportion of cell types in organoids profiled at DIV70 and DIV150 across all control lines. Early radial glia (RG-early, 22%) and differentiated excitatory neurons (EN, 23%) are the predominant cell types. Intermediate progenitors differentiating into new born excitatory neurons represent the next largest group (IPC-nEN, 14%). 5%-10% of the cell population consists of other intermediate cell types, including cycling radial glia (cyc-RG), early new born neurons (nEN-early), late radial glia (RG-late), striatal interneurons (IN-STR) and choroid. A minority (≤5%) of cells are comprised of late newborn neurons (nEN-late), cortical interneurons (IN-CTX), cycling intermediate progenitors (IPC-div), MGE progenitors (MGE-RG, MGE-IPC, MGE-RG_IPC-div) and new born interneurons (nIN). Almost no astroglia is detected at DIV70. By DIV150 organoids display a more diverse distribution of cell types including EN (15.5%), RG-late (12%), cortical interneurons (IN-CTX, 19%), IN-STR (10.5%) as well as astrocytes (0.5%). Other cell types represent less than 5% each. The fraction of cells that are part of the EN lineage decreases from 73% at DIV70 to 33% at DIV150 although the proportion of newborn and maturing EN remains fairly constant (30% at DIV70 vs 23% at DIV150). There is an expansion of IN lineage (from 19% at DIV70 to 56% at DIV150), which includes increase in the proportion of IN progenitors (9% to 21%), as well as newborn and maturing IN (10% to 35%). The relative proportion of choroid cells decreases from 7.7% to 0.8% while the astrocyte proportion increases from 0.1% to 9.5%.

Fig S4: Quantification of the thickness of neurogenic zones and FACS-based cell cycle analysis of organoids.

(a) Representative confocal image (40x) of a rosette structure in 30µm section of DIV45 organoids immunostained for PAX6 (red) and CTIP2 (green). Scale bar = 100µm. **(b)** Schematic

depicting the quantification of the layer thickness in the rosettes. PAX6 layer is defined as the ventricular zone (VZ), CTIP2 layer is defined as the cortical plate (CP) and total neural tube radius is defined as the distance from the center of the ventricle to the top of the CP layer. Measurements of thickness for each layer were made along 3 lines per rosette that are at 45 degrees to each other and average values for relative thickness of each layer compared to the radius of the rosette (neural tube radius) was calculated. **(c)** Quantification of layer thickness in DIV45 organoids. CP layer thickness is significantly decreased in patient organoids (Kolmogorov-Smirnov test, $P = 0.04$; total structures analyzed: n ROIs for control = 16, n for patient = 12 from 3 control and 3 patient lines). **(d)** Representative histogram of FACS data from one control (*left*) and one patient (*right*) organoid suspension labeled with propidium iodide (PI). Fluorescence ratios (488/620PI) defining G0-G1 and actively cycling (S-M) phases are indicated with brackets. **(e)** Quantification of fraction of sorted cells in G0-G1 (left) and active cycling (S-M) phases (*right*) from 3 pairs from 2 independent batches ($P = 0.07$). There is a trend towards higher fraction of cells in active cycling stages in patient compared to control organoids.

Fig S5: Pseudotime analysis of the EN and IN lineages.

(a) Pseudotime trajectory of EN lineage calculated with Monocle3 with cell type annotations. Trajectory starts at cyc-RG and progresses to RG-early, IPC-nEN, then branches into nEN-early and nEN-late and finally to EN. **(b)** Pseudotime trajectory colored by DIV. At DIV70 there are mainly progenitors and neurons in the nEN-early to EN branch. At DIV150 there are fewer early progenitors and mainly neurons in the nEN-late to EN branch. **(c)** Pseudotime trajectory of IN lineage calculated with Monocle3 with cell type annotations. Trajectory starts at RG-late and progresses to MGE RG and MGE IPC, differentiates to nIN , then branches into IN-CTX and IN-STR

Supplementary Tables

Supplementary Table 1: Bulk RNAseq_DEGs in in sorted neurons from DIV70 patient organoids compared to control.

Supplementary Table 2: scRNAseq_DEGs in various cell types of DIV70 patient organoids compared to control.

Supplementary Table 3: scRNAseq_Functional enrichment of DEGs in various cell types of DIV70 patient organoids compared to control.

Supplementary Table 4: scRNAseq_DEGs in various cell types of DIV150 patient organoids compared to control.

Supplementary Table 5: scRNAseq_Functional enrichment of DEGs in various cell types of DIV150 patient organoids compared to control.

Supplementary Table 6: scRNAseq_Functional enrichment of transcription factor regulon targets dysregulated in ENs of DIV70 patient organoids.

Supplementary Table 7: WGCNA EN lineage module genes.

Supplementary Table 8: miRNAseq_Differentially expressed miRNAs in whole patient organoids at DIV70 compared to control.

Supplementary Table 9: Clinical and demographic characteristics of 22q11.2DS/SCZ patients and healthy controls.

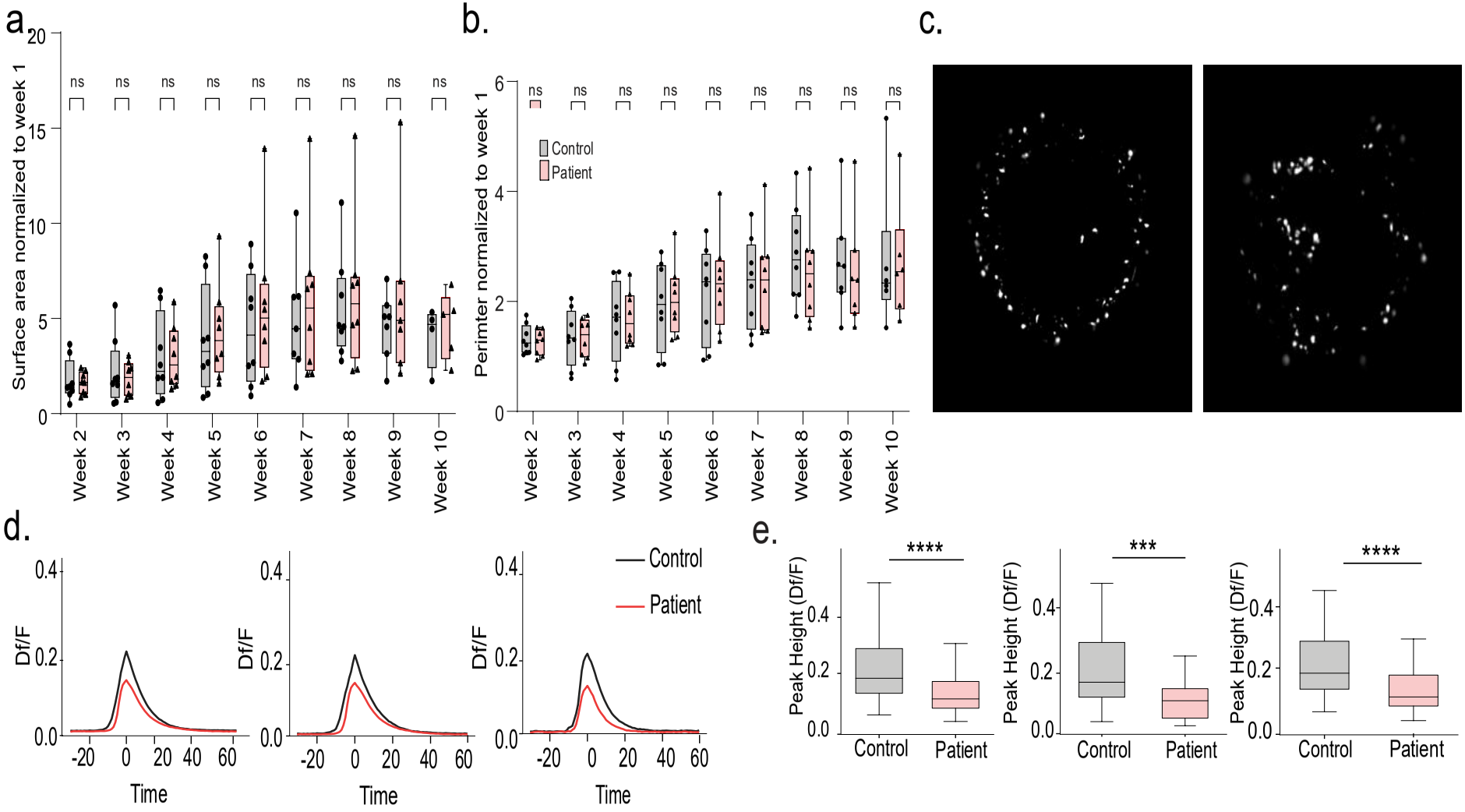
a.
Surface area normalized to week 1
ns
Week 2
Week 3
Week 4
Week 5
Week 6
Week 7
Week 8
Week 9
Week 10
b.
Perimter normalized to week 1
Control
Patient
c.
d.
Df/F
Time
Control
Patient
e.
Peak Height (Df/F)
****
***
****
Control
Patient

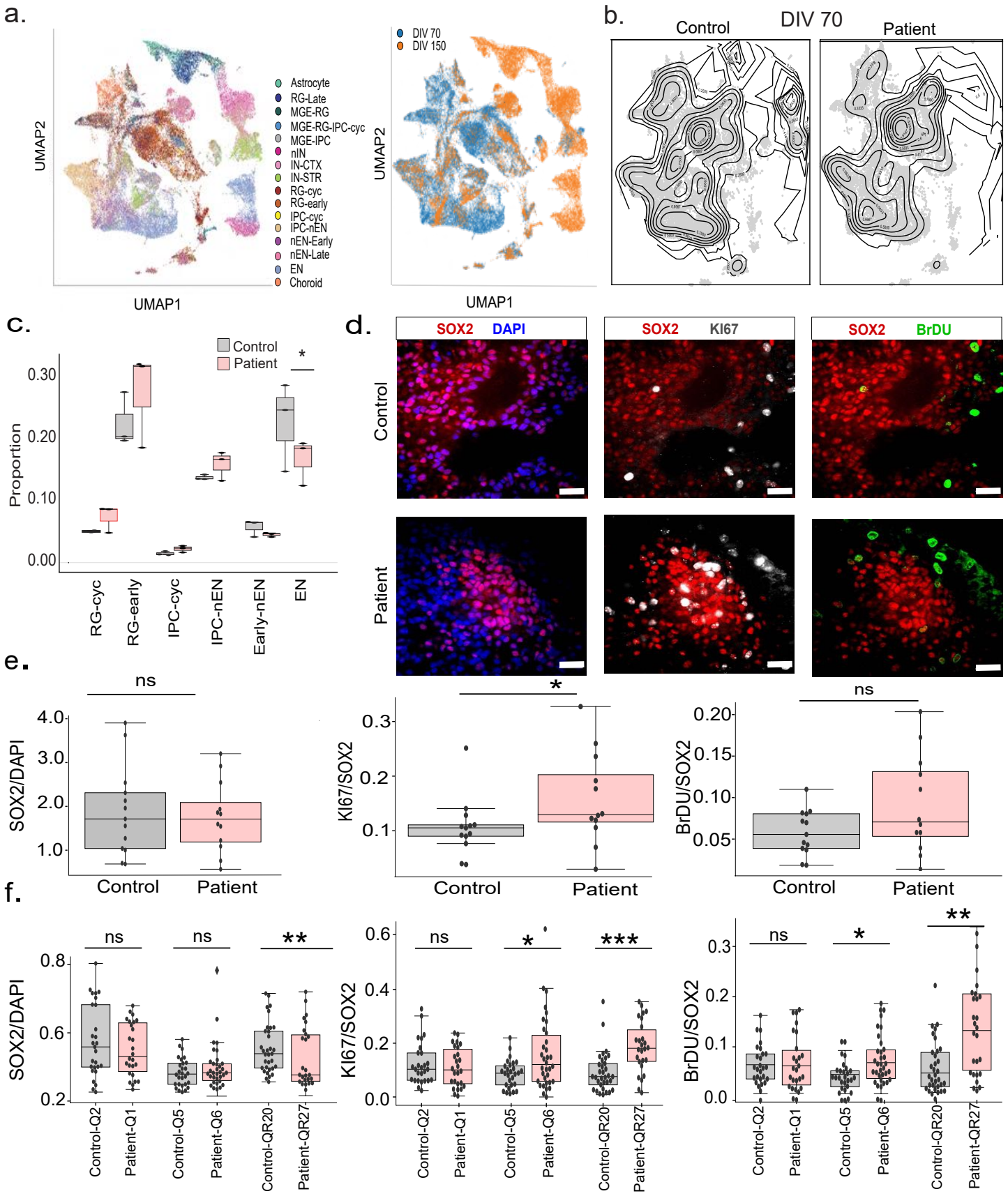
a.
UMAP2
UMAP1
Astrocyte
RG-Late
MGE-RG
MGE-RG-IPC-cyc
MGE-IPC
nIN
IN-CTX
IN-STR
RG-cyc
RG-early
IPC-cyc
IPC-nEN
nEN-Early
nEN-Late
EN
Choroid
DIV 70
DIV 150
b.
Control
DIV 70
Patient
c.
Control
Patient
Proportion
RG-cyc
RG-early
IPC-cyc
IPC-nEN
Early-nEN
EN
d.
SOX2
DAPI
KI67
BrDU
Control
Patient
e.
SOX2/DAPI
KI67/SOX2
BrDU/SOX2
ns
Control
Patient
f.
Control-Q2
Patient-Q1
Control-Q5
Patient-Q6
Control-QR20
Patient-QR27

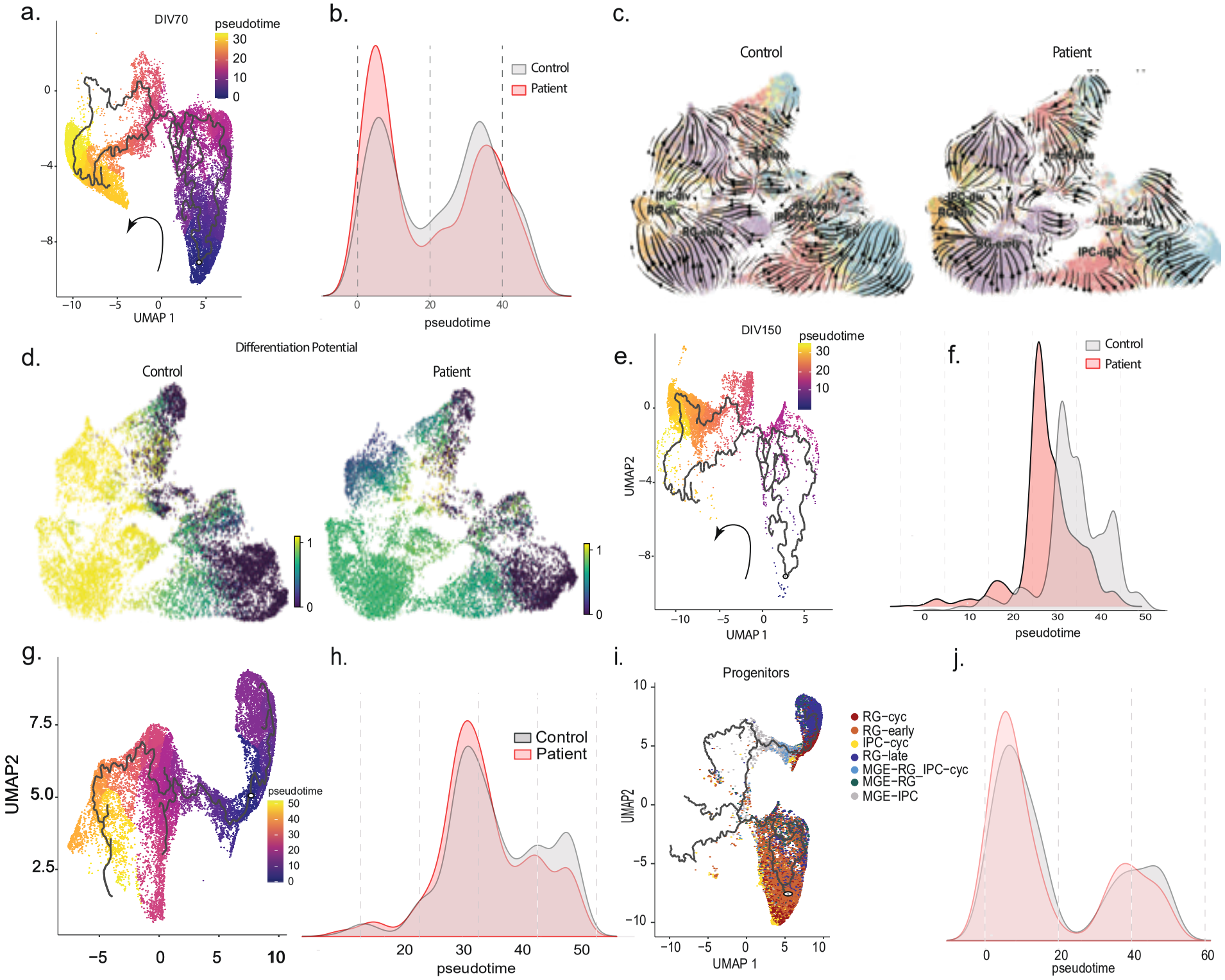
a.
DIV70
pseudotime
30
20
10
0
0
−4
−8
−10
−5
0
5
UMAP 1
b.
Control
Patient
0
20
40
pseudotime
c.
Control
Patient
IPC-div
RG-div
RG-early
IPC-nEN
nEN-early
EN
nEN-late
d.
Differentiation Potential
Control
Patient
1
0
e.
DIV150
pseudotime
30
20
10
UMAP2
UMAP 1
f.
Control
Patient
0
10
20
30
40
50
pseudotime
g.
UMAP2
7.5
5.0
2.5
pseudotime
50
40
30
20
10
0
−5
0
5
10
h.
Control
Patient
20
30
40
50
pseudotime
i.
Progenitors
UMAP2
UMAP 1
RG−cyc
RG−early
IPC−cyc
RG−late
MGE−RG_IPC−cyc
MGE−RG
MGE−IPC
j.
0
20
40
60
pseudotime

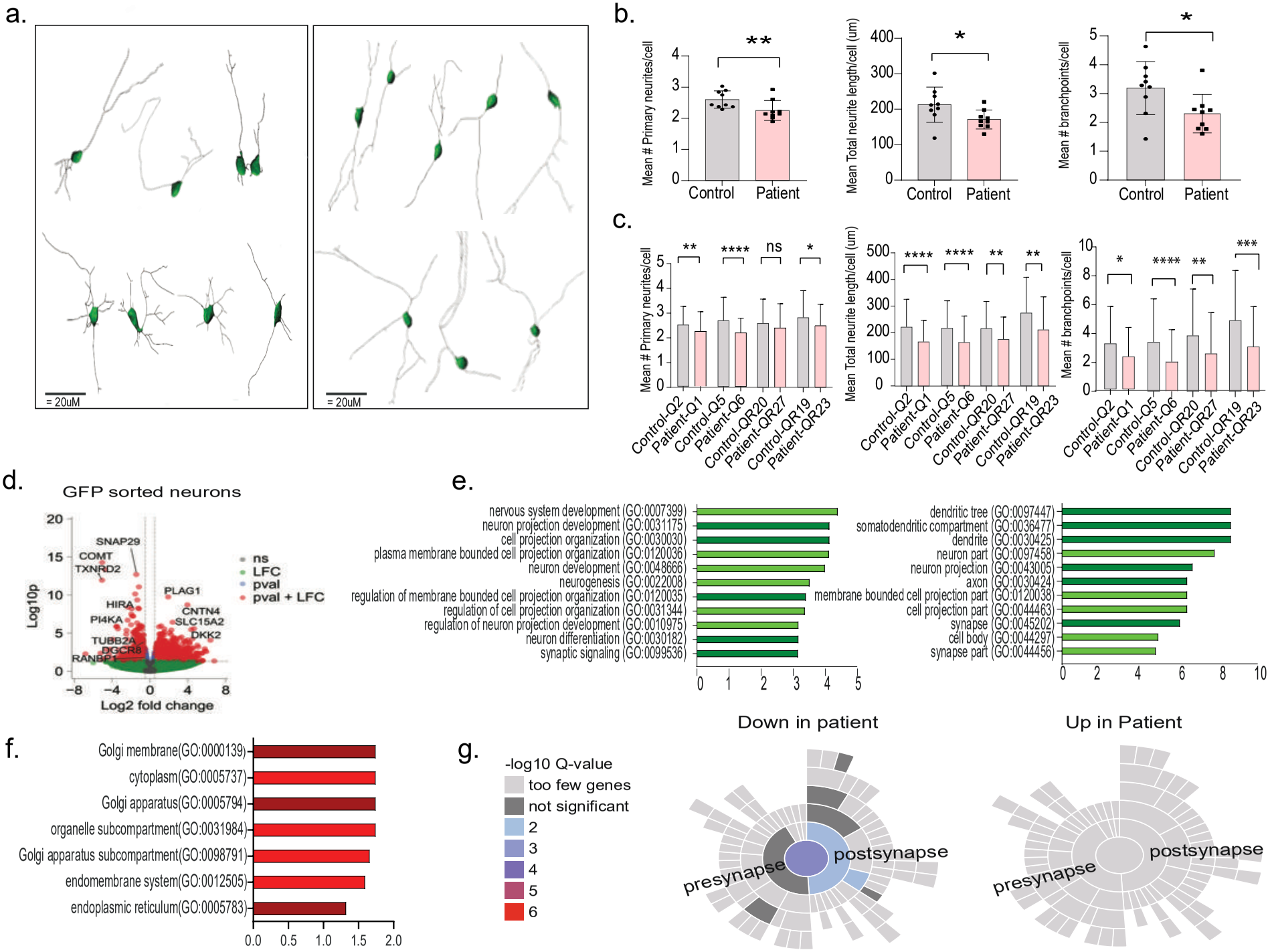
a.
= 20uM
= 20uM
b.
Mean # Primary neurites/cell
Mean Total neurite length/cell (um)
Mean # branchpoints/cell
Control
Patient
c.
Control-Q2
Patient-Q1
Control-Q5
Patient-Q6
Control-QR20
Patient-QR27
Control-QR19
Patient-QR23
d.
GFP sorted neurons
Log10p
Log2 fold change
ns
LFC
pval
pval + LFC
SNAP29
COMT
TXNRD2
PLAG1
HIRA
CNTN4
PI4KA
SLC15A2
DKK2
TUBB2A
DGCR8
RANBP1
e.
nervous system development (GO:0007399)
neuron projection development (GO:0031175)
cell projection organization (GO:0030030)
plasma membrane bounded cell projection organization (GO:0120036)
neuron development (GO:0048666)
neurogenesis (GO:0022008)
regulation of membrane bounded cell projection organization (GO:0120035)
regulation of cell projection organization (GO:0031344)
regulation of neuron projection development (GO:0010975)
neuron differentiation (GO:0030182)
synaptic signaling (GO:0099536)
dendritic tree (GO:0097447)
somatodendritic compartment (GO:0036477)
dendrite (GO:0030425)
neuron part (GO:0097458)
neuron projection (GO:0043005)
axon (GO:0030424)
membrane bounded cell projection part (GO:0120038)
cell projection part (GO:0044463)
synapse (GO:0045202)
cell body (GO:0044297)
synapse part (GO:0044456)
Down in patient
Up in Patient
f.
Golgi membrane(GO:0000139)
cytoplasm(GO:0005737)
Golgi apparatus(GO:0005794)
organelle subcompartment(GO:0031984)
Golgi apparatus subcompartment(GO:0098791)
endomembrane system(GO:0012505)
endoplasmic reticulum(GO:0005783)
g.
-log10 Q-value
too few genes
not significant
2
3
4
5
6
presynapse
postsynapse
presynapse
postsynapse

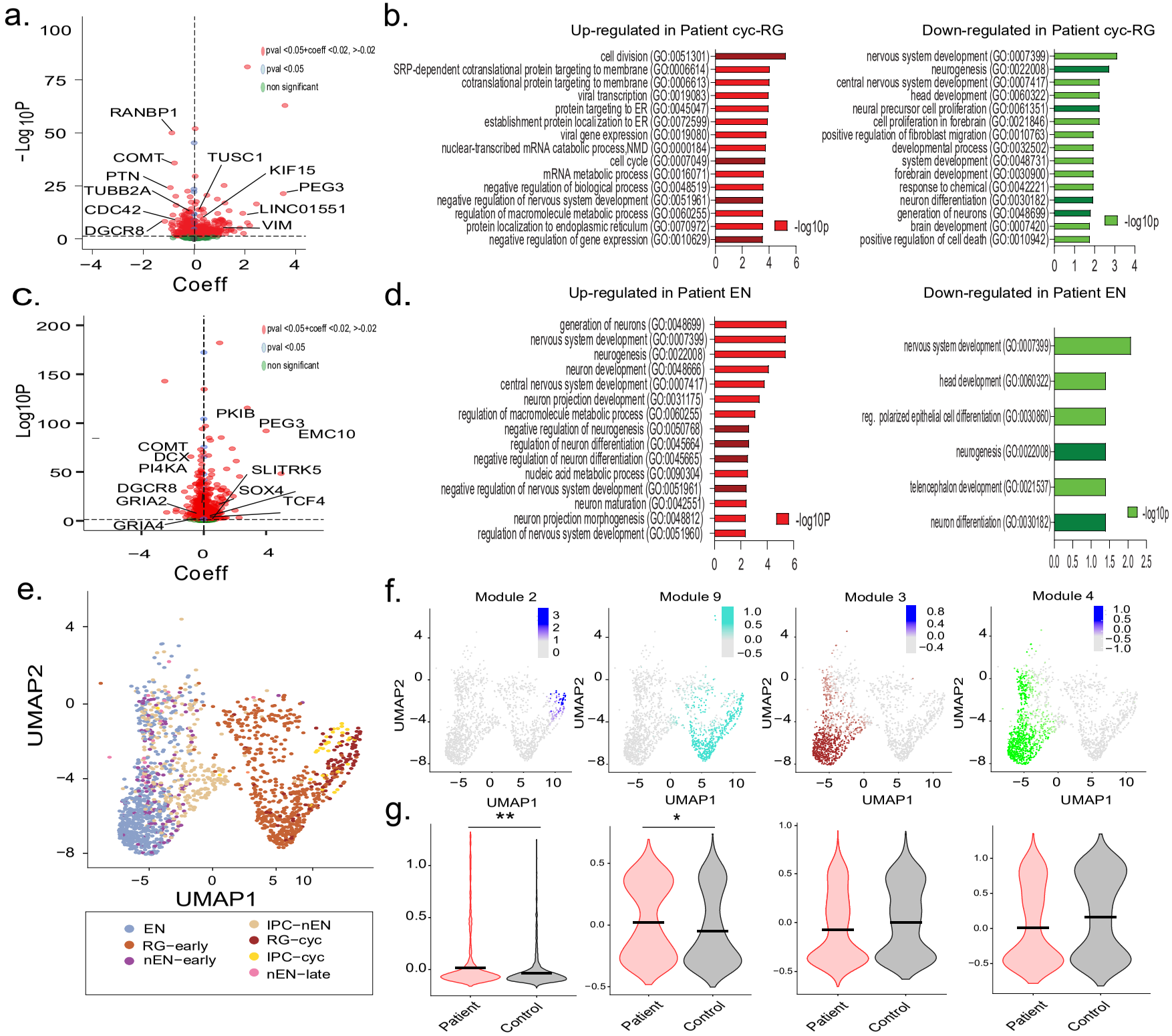
a.
pval <0.05+coeff <0.02, >-0.02
pval <0.05
non significant
-Log10P
Coeff
RANBP1
COMT
TUSC1
KIF15
PTN
TUBB2A
PEG3
CDC42
LINC01551
DGCR8
VIM
b.
Up-regulated in Patient cyc-RG
cell division (GO:0051301)
SRP-dependent cotranslational protein targeting to membrane (GO:0006614)
cotranslational protein targeting to membrane (GO:0006613)
viral transcription (GO:0019083)
protein targeting to ER (GO:0045047)
establishment protein localization to ER (GO:0072599)
viral gene expression (GO:0019080)
nuclear-transcribed mRNA catabolic process,NMD (GO:0000184)
cell cycle (GO:0007049)
mRNA metabolic process (GO:0016071)
negative regulation of biological process (GO:0048519)
negative regulation of nervous system development (GO:0051961)
regulation of macromolecule metabolic process (GO:0060255)
protein localization to endoplasmic reticulum (GO:0070972)
negative regulation of gene expression (GO:0010629)
-log10p
Down-regulated in Patient cyc-RG
nervous system development (GO:0007399)
neurogenesis (GO:0022008)
central nervous system development (GO:0007417)
head development (GO:0060322)
neural precursor cell proliferation (GO:0061351)
cell proliferation in forebrain (GO:0021846)
positive regulation of fibroblast migration (GO:0010763)
developmental process (GO:0032502)
system development (GO:0048731)
forebrain development (GO:0030900)
response to chemical (GO:0042221)
neuron differentiation (GO:0030182)
generation of neurons (GO:0048699)
brain development (GO:0007420)
positive regulation of cell death (GO:0010942)
-log10p
c.
pval <0.05+coeff <0.02, >-0.02
pval <0.05
non significant
Log10P
Coeff
PKIB
PEG3
EMC10
COMT
DCX
PI4KA
SLITRK5
DGCR8
SOX4
GRIA2
TCF4
GRIA4
d.
Up-regulated in Patient EN
generation of neurons (GO:0048699)
nervous system development (GO:0007399)
neurogenesis (GO:0022008)
neuron development (GO:0048666)
central nervous system development (GO:0007417)
neuron projection development (GO:0031175)
regulation of macromolecule metabolic process (GO:0060255)
negative regulation of neurogenesis (GO:0050768)
regulation of neuron differentiation (GO:0045664)
negative regulation of neuron differentiation (GO:0045665)
nucleic acid metabolic process (GO:0090304)
negative regulation of nervous system development (GO:0051961)
neuron maturation (GO:0042551)
neuron projection morphogenesis (GO:0048812)
regulation of nervous system development (GO:0051960)
-log10P
Down-regulated in Patient EN
nervous system development (GO:0007399)
head development (GO:0060322)
reg. polarized epithelial cell differentiation (GO:0030860)
neurogenesis (GO:0022008)
telencephalon development (GO:0021537)
neuron differentiation (GO:0030182)
-log10p
e.
UMAP2
UMAP1
EN
RG-early
nEN-early
IPC-nEN
RG-cyc
IPC-cyc
nEN-late
f.
Module 2
Module 9
Module 3
Module 4
UMAP2
UMAP1
g.
**
*
Patient
Control

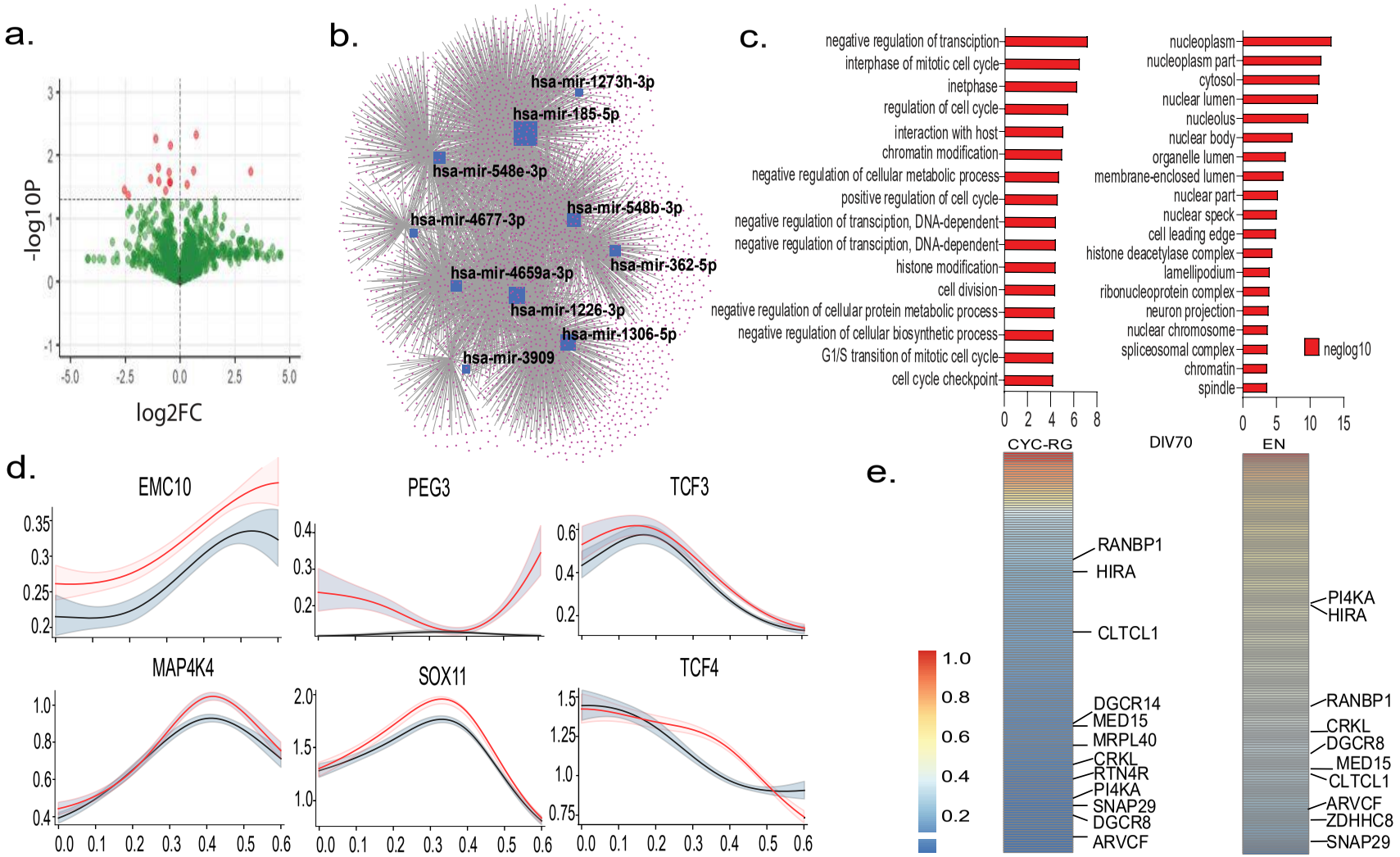
a.
-log10P
log2FC
b.
hsa-mir-1273h-3p
hsa-mir-185-5p
hsa-mir-548e-3p
hsa-mir-548b-3p
hsa-mir-4677-3p
hsa-mir-362-5p
hsa-mir-4659a-3p
hsa-mir-1226-3p
hsa-mir-1306-5p
hsa-mir-3909
c.
negative regulation of transcription
interphase of mitotic cell cycle
inetphase
regulation of cell cycle
interaction with host
chromatin modification
negative regulation of cellular metabolic process
positive regulation of cell cycle
negative regulation of transcription, DNA-dependent
negative regulation of transcription, DNA-dependent
histone modification
cell division
negative regulation of cellular protein metabolic process
negative regulation of cellular biosynthetic process
G1/S transition of mitotic cell cycle
cell cycle checkpoint
nucleoplasm
nucleoplasm part
cytosol
nuclear lumen
nucleolus
nuclear body
organelle lumen
membrane-enclosed lumen
nuclear part
nuclear speck
cell leading edge
histone deacetylase complex
lamellipodium
ribonucleoprotein complex
neuron projection
nuclear chromosome
spliceosomal complex
chromatin
spindle
neglog10
d.
EMC10
PEG3
TCF3
MAP4K4
SOX11
TCF4
e.
CYC-RG
DIV70
EN
RANBP1
HIRA
CLTCL1
DGCR14
MED15
MRPL40
CRKL
RTN4R
PI4KA
SNAP29
DGCR8
ARVCF
PI4KA
HIRA
RANBP1
CRKL
DGCR8
MED15
CLTCL1
ARVCF
ZDHHC8
SNAP29

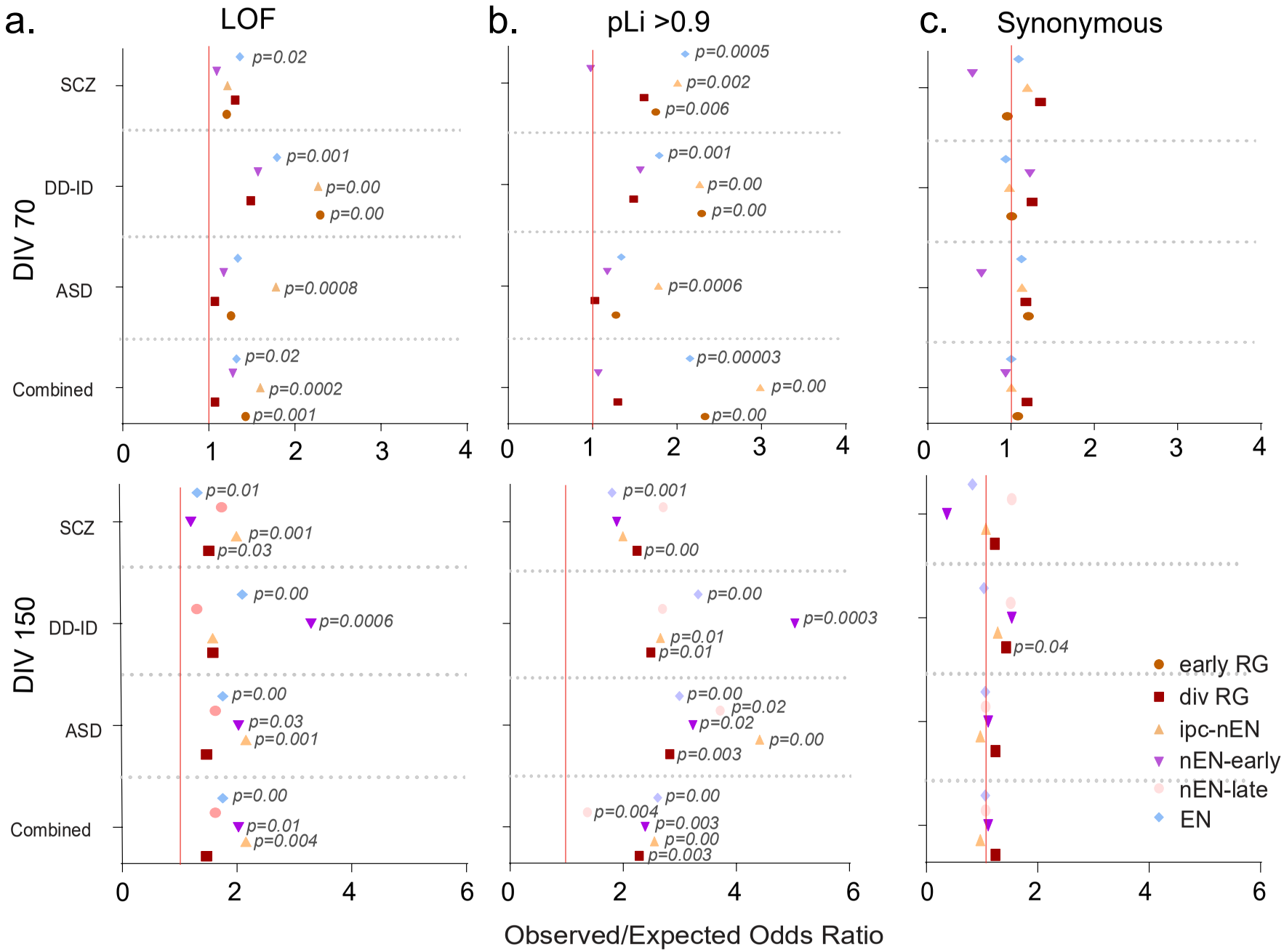
a.
LOF
b.
pLi >0.9
c.
Synonymous
DIV 70
DIV 150
SCZ
DD-ID
ASD
Combined
p=0.02
p=0.001
p=0.00
p=0.00
p=0.0008
p=0.02
p=0.0002
p=0.001
p=0.0005
p=0.002
p=0.006
p=0.001
p=0.00
p=0.00
p=0.0006
p=0.00003
p=0.00
p=0.00
p=0.01
p=0.001
p=0.03
p=0.00
p=0.0006
p=0.00
p=0.03
p=0.001
p=0.00
p=0.01
p=0.004
p=0.001
p=0.00
p=0.00
p=0.0003
p=0.01
p=0.01
p=0.00
p=0.02
p=0.02
p=0.00
p=0.003
p=0.00
p=0.004
p=0.003
p=0.00
p=0.003
p=0.04
early RG
div RG
ipc-nEN
nEN-early
nEN-late
EN
0
1
2
3
4
6
Observed/Expected Odds Ratio

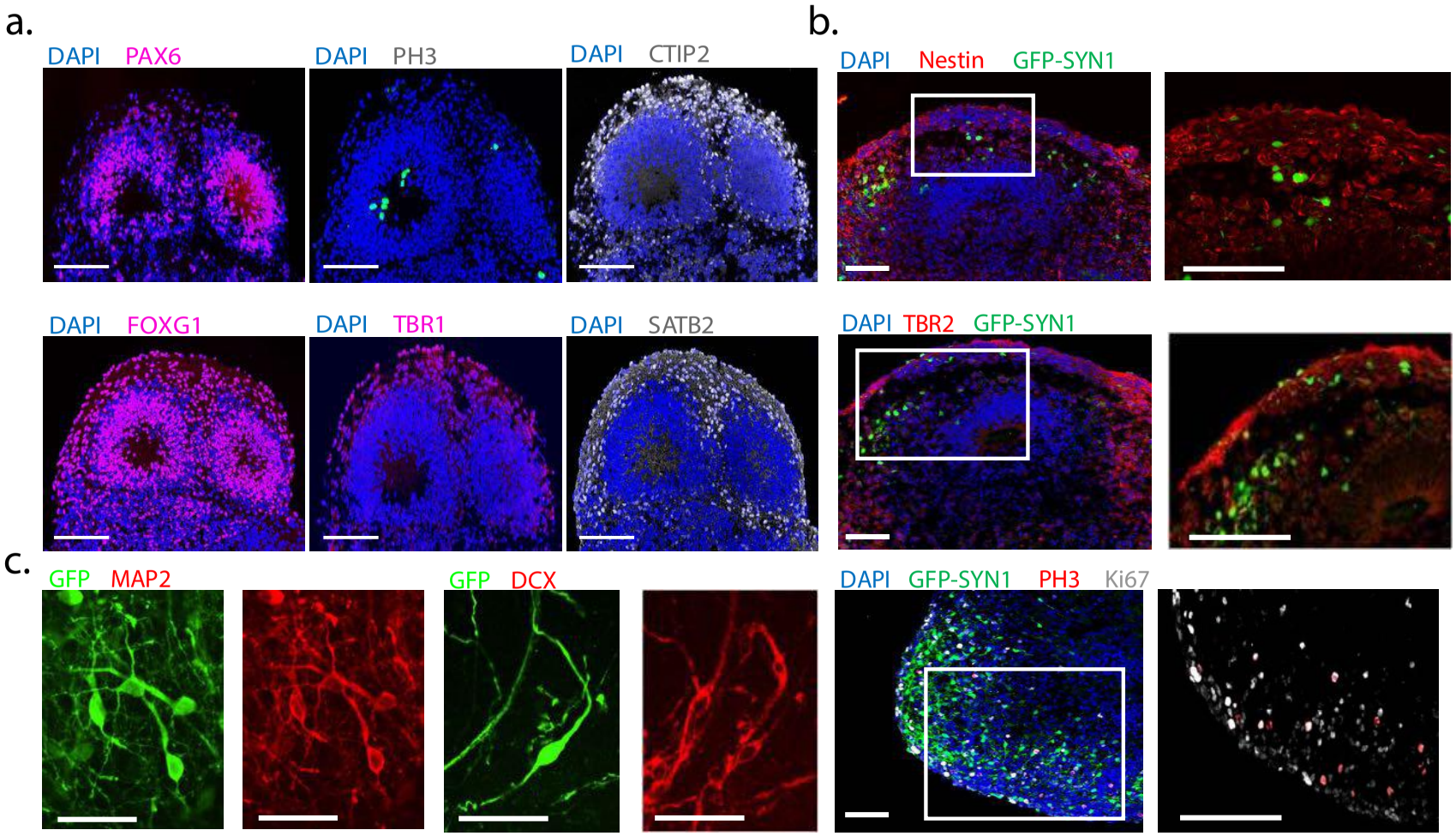
a.
DAPI PAX6
DAPI PH3
DAPI CTIP2
DAPI FOXG1
DAPI TBR1
DAPI SATB2
b.
DAPI Nestin GFP-SYN1
DAPI TBR2 GFP-SYN1
c.
GFP MAP2
GFP DCX
DAPI GFP-SYN1 PH3 Ki67

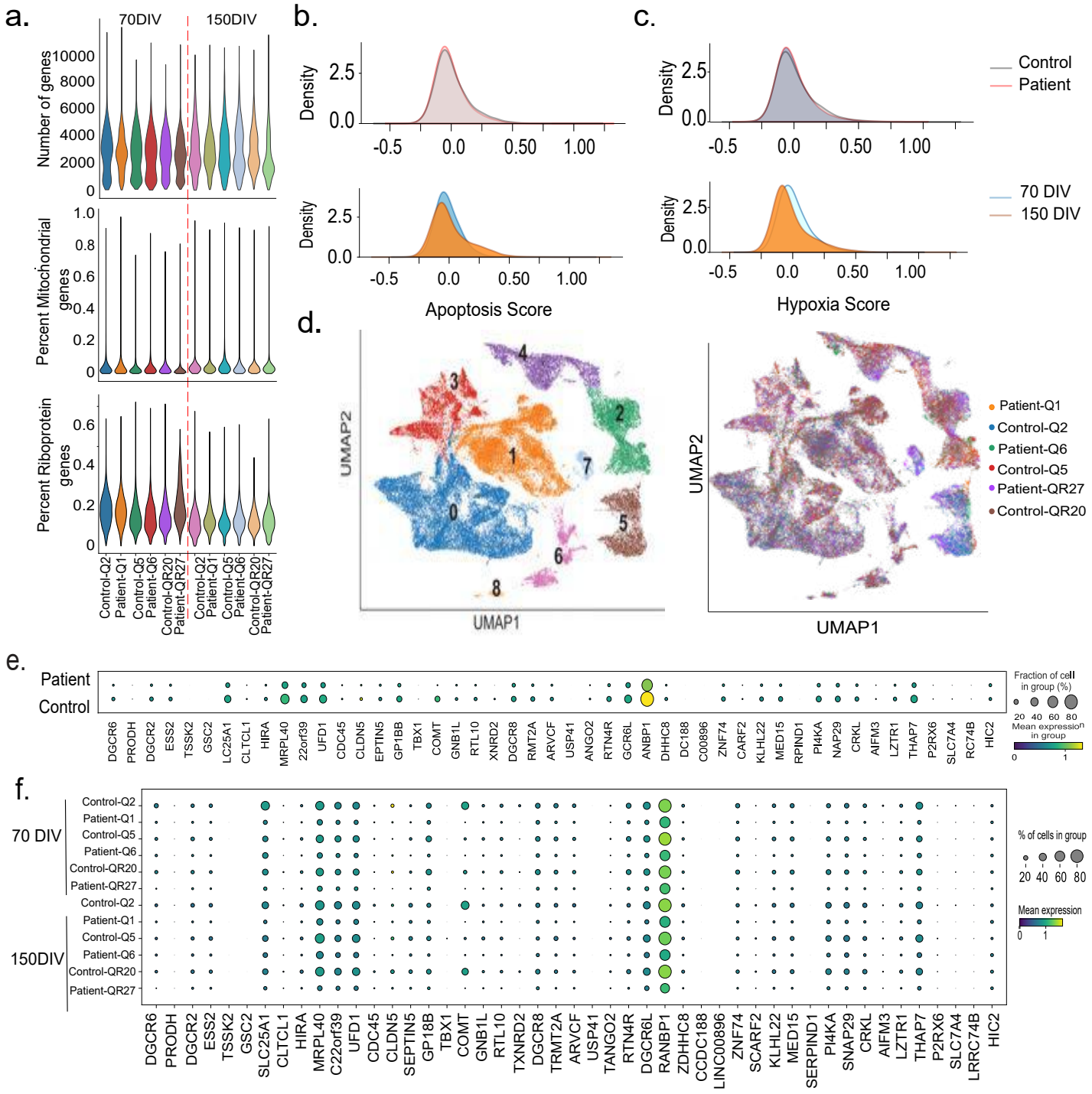
a.
70DIV
150DIV
Number of genes
Percent Mitochondrial genes
Percent Riboprotein genes
Control-Q2
Patient-Q1
Control-Q5
Patient-Q6
Control-QR20
Patient-QR27
b.
Density
Apoptosis Score
c.
Control
Patient
70 DIV
150 DIV
Hypoxia Score
d.
UMAP2
UMAP1
Patient-Q1
Control-Q2
Patient-Q6
Control-Q5
Patient-QR27
Control-QR20
e.
Patient
Control
Fraction of cell in group (%)
Mean expression in group
f.
70 DIV
150DIV
% of cells in group
Mean expression

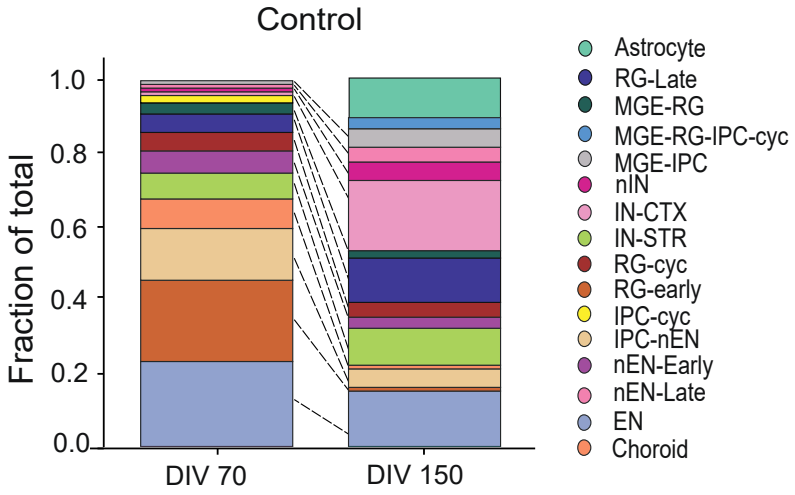
Control
Fraction of total
1.0
0.8
0.6
0.4
0.2
0.0
DIV 70
DIV 150
Astrocyte
RG-Late
MGE-RG
MGE-RG-IPC-cyc
MGE-IPC
nIN
IN-CTX
IN-STR
RG-cyc
RG-early
IPC-cyc
IPC-nEN
nEN-Early
nEN-Late
EN
Choroid

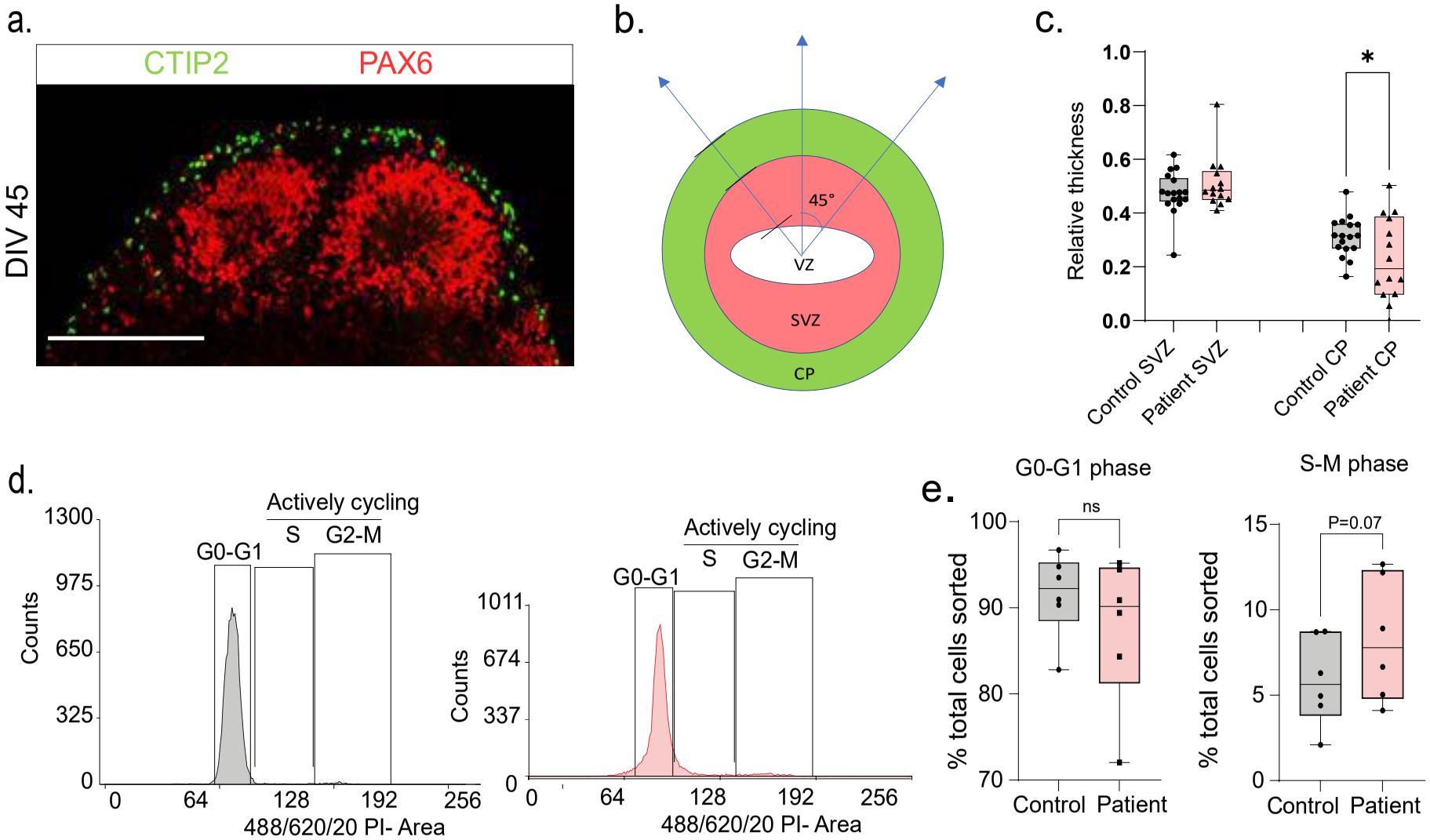
a.
CTIP2
PAX6
DIV 45
b.
45°
VZ
SVZ
CP
c.
Relative thickness
1.0
0.8
0.6
0.4
0.2
0.0
*
Control SVZ
Patient SVZ
Control CP
Patient CP
d.
Actively cycling
S
G2-M
G0-G1
Counts
1300
975
650
325
0
0
64
128
192
256
488/620/20 PI- Area
1011
674
337
e.
G0-G1 phase
S-M phase
ns
P=0.07
% total cells sorted
100
90
80
70
15
10
5
Control
Patient

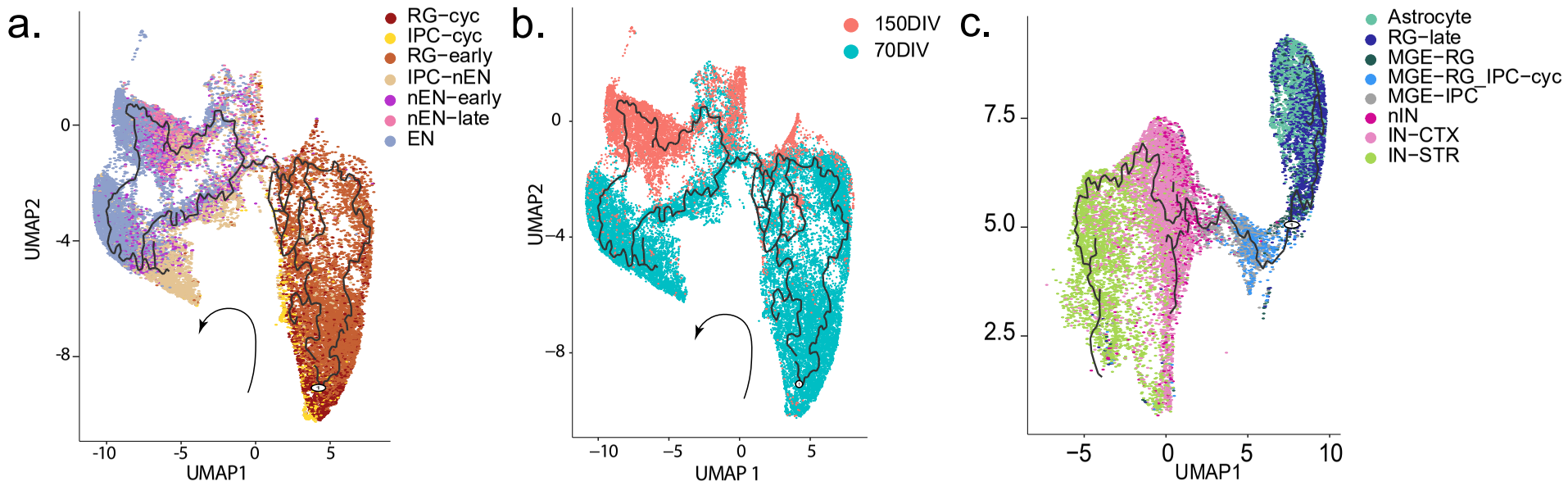
a.
RG−cyc
IPC−cyc
RG−early
IPC−nEN
nEN−early
nEN−late
EN
UMAP2
UMAP1
b.
150DIV
70DIV
UMAP2
UMAP 1
c.
Astrocyte
RG−late
MGE−RG
MGE−RG_IPC−cyc
MGE−IPC
nIN
IN−CTX
IN−STR
UMAP1